










TECH BRIEFS

NATIONAL AERONAUTICS AND SPACE ADMINISTRATION

-  **Technology Focus**
-  **Electronics/Computers**
-  **Software**
-  **Materials**
-  **Mechanics/Machinery**
-  **Manufacturing**
-  **Bio-Medical**
-  **Physical Sciences**
-  **Information Sciences**
-  **Books and Reports**

INTRODUCTION

Tech Briefs are short announcements of innovations originating from research and development activities of the National Aeronautics and Space Administration. They emphasize information considered likely to be transferable across industrial, regional, or disciplinary lines and are issued to encourage commercial application.

Availability of NASA Tech Briefs and TSPs

Requests for individual Tech Briefs or for Technical Support Packages (TSPs) announced herein should be addressed to

National Technology Transfer Center

Telephone No. (800) 678-6882 or via World Wide Web at www.nttc.edu

Please reference the control numbers appearing at the end of each Tech Brief. Information on NASA's Innovative Partnerships Program (IPP), its documents, and services is also available at the same facility or on the World Wide Web at <http://ipp.nasa.gov>.

Innovative Partnerships Offices are located at NASA field centers to provide technology-transfer access to industrial users. Inquiries can be made by contacting NASA field centers listed below.

NASA Field Centers and Program Offices

Ames Research Center

Lisa L. Lockyer
(650) 604-1754
lisa.l.lockyer@nasa.gov

Dryden Flight Research Center

Gregory Poteat
(661) 276-3872
greg.poteat@dfrc.nasa.gov

Glenn Research Center

Kathy Needham
(216) 433-2802
kathleen.k.needham@nasa.gov

Goddard Space Flight Center

Nona Cheeks
(301) 286-5810
nona.k.cheeks@nasa.gov

Jet Propulsion Laboratory

Ken Wolfenbarger
(818) 354-3821
james.k.wolfenbarger@jpl.nasa.gov

Johnson Space Center

Michele Brekke
(281) 483-4614
michele.a.brekke@nasa.gov

Kennedy Space Center

David R. Makufka
(321) 867-6227
david.r.makufka@nasa.gov

Langley Research Center

Martin Waszak
(757) 864-4015
martin.r.waszak@nasa.gov

Marshall Space Flight Center

Jim Dowdy
(256) 544-7604
jim.dowdy@msfc.nasa.gov

Stennis Space Center

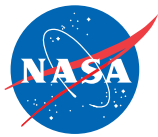
John Bailey
(228) 688-1660
john.w.bailey@nasa.gov

Carl Ray, Program Executive

Small Business Innovation
Research (SBIR) & Small
Business Technology
Transfer (STTR) Programs
(202) 358-4652
carl.g.ray@nasa.gov

Doug Comstock, Director

Innovative Partnerships
Program Office
(202) 358-2560
doug.comstock@nasa.gov



TECH BRIEFS

NATIONAL AERONAUTICS AND SPACE ADMINISTRATION



- 5 Technology Focus: Test & Measurement**
- 5 Wireless Measurement of Contact and Motion Between Contact Surfaces
 - 5 Wireless Measurement of Rotation and Displacement Rate
 - 6 Portable Microleak-Detection System
 - 7 Free-to-Roll Testing of Airplane Models in Wind Tunnels
 - 8 Cryogenic Shrouds for Testing Thermal-Insulation Panels



- 9 Electronics/Computers**
- 9 Optoelectronic System Measures Distances to Multiple Targets
 - 10 Tachometers Derived From a Brushless DC Motor



- 13 Software**
- 13 Algorithm-Based Fault Tolerance for Numerical Subroutines
 - 13 Computational Support for Technology-Investment Decisions
 - 13 DSN Resource Scheduling
 - 13 Distributed Operations Planning



- 15 Mechanics/Machinery**
- 15 Phase-Oriented Gear Systems



- 17 Manufacturing & Prototyping**
- 17 Freeze Tape Casting of Functionally Graded Porous Ceramics
 - 18 Electrophoretic Deposition on Porous Non-Conductors



- 21 Bio-Medical**
- 21 Two Devices for Removing Sludge From Bioreactor Wastewater
 - 22 Portable Unit for Metabolic Analysis



- 23 Physical Sciences**
- 23 Flash Diffusivity Technique Applied to Individual Fibers
 - 24 System for Thermal Imaging of Hot Moving Objects
 - 25 Large Solar-Rejection Filter
 - 25 Improved Readout Scheme for SQUID-Based Thermometry



- 27 Information Sciences**
- 27 Error Rates and Channel Capacities in Multipulse PPM
 - 28 Two Mathematical Models of Nonlinear Vibrations
 - 28 Simpler Adaptive Selection of Golomb Power-of-Two Codes



- 31 Books & Reports**
- 31 VCO PLL Frequency Synthesizers for Spacecraft Transponders
 - 31 Wide Tuning Capability for Spacecraft Transponders
 - 31 Adaptive Deadband Synchronization for a Spacecraft Formation
 - 31 Analysis of Performance of Stereoscopic-Vision Software
 - 32 Estimating the Inertia Matrix of a Spacecraft
 - 32 Spatial Coverage Planning for Exploration Robots
 - 32 Increasing the Life of a Xenon-Ion Spacecraft Thruster

This document was prepared under the sponsorship of the National Aeronautics and Space Administration. Neither the United States Government nor any person acting on behalf of the United States Government assumes any liability resulting from the use of the information contained in this document, or warrants that such use will be free from privately owned rights.



Wireless Measurement of Contact and Motion Between Contact Surfaces

A magnetic-field-response contact sensor is used.

Langley Research Center, Hampton, Virginia

This method uses a magnetic-field-response contact sensor that is designed to identify surface contact and motion between contact locations. The sensor has three components: (1) a capacitor-inductor circuit with two sets of electrical contact pads, (2) a capacitor with a set of electrical contact pads, and (3) an inductor with a set of electrical contact pads. A unique feature of this sensor is that it is inherently multifunctional. Information can be derived from analyzing such sensor response attributes as amplitude, frequency, and bandwidth. A change in one attribute can be due to a change in a

physical property of a system. A change in another attribute can be due to another physical property, which has no relationship to the first one.

The sensor is powered and interrogated without physical connection to a power source, microprocessor, data acquisition equipment, or electrical circuitry. It works with the magnetic-field-response recorder described in "Magnetic-Field-Response Measurement-Acquisition System," *NASA Tech Briefs*, Vol. 30, No. 6 (June 2006), page 28.

The sensor (capacitor-inductor circuit) is placed on the moving object as

shown in the figure. When contact is made between stationary surface A, the capacitor and the capacitor-inductor circuit form a circuit the response frequency of which is

$$\omega = \frac{1}{2\pi\sqrt{2LC}}$$

The contact pads could be compressible or spring-loaded electrical contacts that are electrically connected to the sensor. Movement away from surface A to the next surface results in the sensor response frequency shifting to

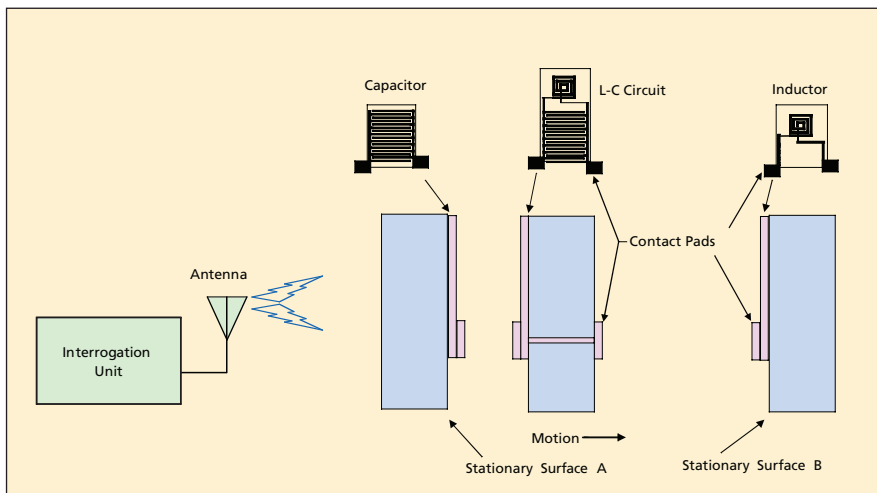
$$\omega = \frac{1}{2\pi\sqrt{LC}}$$

The response amplitude decreases as the sensor moves away from the antenna. Contact with surface B shifts the sensor response frequency to

$$\omega = \frac{1}{2\pi} \sqrt{\frac{2}{LC}}$$

Applications for this include being able to tell whether doors or hatches are sealed, surface bonds are secure (tile bonds, rubber bond to steel belts of tires, etc.), general knowledge of contact between two surfaces, or separation of surfaces.

This work was done by Stanley E. Woodard of Langley Research Center and Bryant D. Taylor of Swales Aerospace. Further information is contained in a TSP (see page 1). LAR-16849-1



Edge View of Object is shown moving away from surface A toward surface B. Surface A has a capacitor with electrical contact pads. Surface B has an inductor with contact pads. The moving object has an inductor-capacitor circuit with two sets of contacts pads to complete the electrical connection with either surface.

Wireless Measurement of Rotation and Displacement Rate

A magnetic field response sensor is used in these measurements.

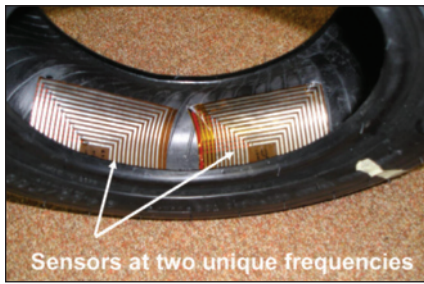
Langley Research Center, Hampton, Virginia

A magnetic field response sensor is designed to measure displacement or rotation rate without a physical connection to a power source, microprocessor, data acquisition equipment, or electrical circuitry. The sensor works with the

magnetic field response recorder, which was described in "Magnetic-Field-Response Measurement-Acquisition System," *NASA Tech Briefs*, Vol. 30, No. 6 (June 2006), page 28. These sensors are wirelessly powered and interrogated,

and the measurement acquisition system and sensors are extremely lightweight.

The response recorder uses oscillating magnetic fields to power the sensors. Once powered, the sensors respond with



Two Response Sensors with different resonant frequencies are sown inside of wheel.

their own magnetic field. For displacement/rotation measurements, the response recorder uses the sensor's response amplitude, which is dependent on the distance from the antenna. The

recorder's antenna orientation and position are kept fixed, and the sampling period is constant.

A sensor with fixed frequency and fixed orientation with respect to the response recorder antenna can be used for position and displacement measurements. If the sensor's orientation is not fixed, but its trajectory is known, it may be possible to calibrate the response amplitude variation with trajectory. For rotational motion such as wheel speed, identifying the number of times the response amplitude exceeds threshold amplitude in a fixed time duration can be used to determine rotation rate. A wheel speed sensor is shown in the figure. The sensor is a thin-film circuit

placed inside the wall of a tire. As the sensor approaches the antenna, the amplitude increases. The amplitude peaks at the closest point to the antenna then decreases producing changes in amplitude that are cyclical. When two sensors with different respond frequencies are used inside the wheel, rotation direction can be determined by identifying which sensor's amplitude increases first. In addition, there is no mechanical wear because no gears are used in the design.

This work was done by Stanley E. Woodard of Langley Research Center and Bryant D. Taylor of Swales Aerospace. Further information is contained in a TSP (see page 1). LAR-16848-1

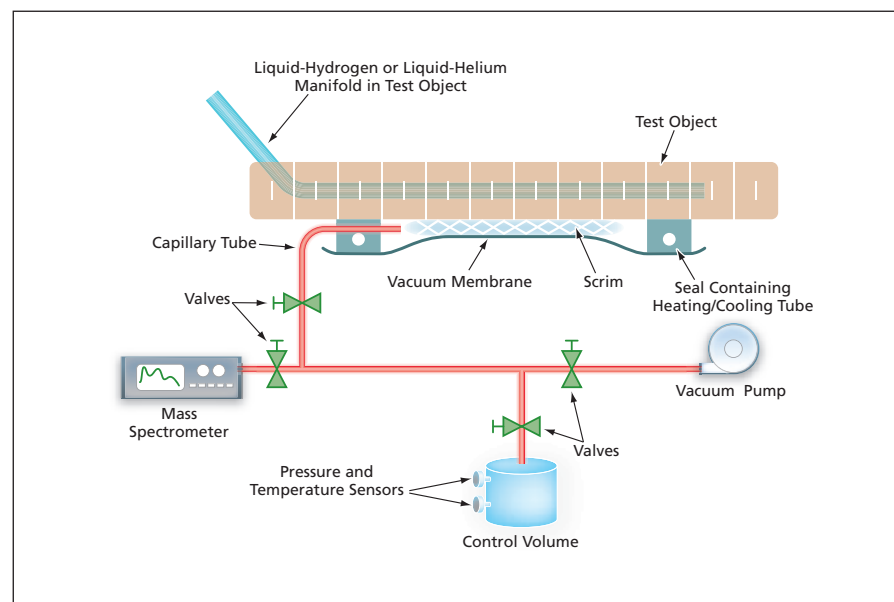
Portable Microleak-Detection System

Heating or cooling of a vacuum seal enables testing over a wide temperature range.

Langley Research Center, Hampton, Virginia

The figure schematically depicts a portable microleak-detection system that has been built especially for use in testing hydrogen tanks made of polymer-matrix composite materials. (As used here, "microleak" signifies a leak that is too small to be detectable by the simple soap-bubble technique.) The system can also be used to test for microleaks in tanks that are made of other materials and that contain gases other than hydrogen. Results of calibration tests have shown that measurement errors are less than 10 percent for leak rates ranging from 0.3 to 200 cm³/min.

Like some other microleak-detection systems, this system includes a vacuum pump and associated plumbing for sampling the leaking gas, and a mass spectrometer for analyzing the molecular constituents of the gas. The system includes a flexible vacuum chamber that can be attached to the outer surface of a tank or other object of interest that is to be tested for leakage (hereafter denoted, simply, the test object). The gas used in a test can be the gas or vapor (e.g., hydrogen in the original application) to be contained by the test object. Alternatively, following common practice in leak testing, helium can be used as a test gas. In either case, the mass spectrometer can be used to verify that the gas measured by the system is the test gas rather than a different gas and, hence, that the leak is indeed from the test object.



The **Portable Microleak-Detection System** includes components in common with prior microleak-detection systems, plus a seal-heating/cooling subsystem that enables testing over a wide temperature range.

The flexibility of the chamber makes it adaptable to test objects having a variety of simple or complex shapes. The flexible vacuum chamber includes an aluminized polyethylene terephthalate vacuum membrane that is sealed to the outer surface of the test object by a flexible, adhesive seal material. A scrim is placed between the inner surface of the membrane and the outer surface of the test object to maintain a gap to accommodate the flow of any leaking gas. A capillary tube that passes through the

seal connects the gap volume with the plumbing that leads to the mass spectrometer, the vacuum pump, and a control volume described next.

The control volume has a known size and is instrumented with pressure and temperature sensors. In use, the control volume is evacuated, then disconnected from the vacuum pump, and then the pressure and temperature are measured as the leaking gas flows into the control volume. By use of the ideal-gas law, the rate of leakage can be calculated from

the temperature and measured rate of increase of pressure.

An unusual feature of this system is a heating/cooling subsystem that includes a tube embedded in the flexible adhesive seal. A heating or cooling liquid can be circulated through this tube to maintain the seal at or near room temperature, where it is most effective,

regardless of the temperature of the test object or the environment. The heating/cooling subsystem is essential, for example, for maintaining an effective seal for testing a tank, pipe, valve, or other object that contains liquid hydrogen or other cryogenic fluid. The heated/cooled seal enables testing at temperatures from -455 to $+350$ °F

(about -271 to $+177$ °C), even in the presence of distortions caused by mechanical and thermal loads applied to the test object.

This work was done by H. Kevin Rivers and Joseph G Sikora of Langley Research Center and Sankara N. Sankaran of Lockheed Martin Space Operations. Further information is contained in a TSP (see page 1). LAR-16139

Free-to-Roll Testing of Airplane Models in Wind Tunnels

Causes of, and cures for, wing-drop/rock behavior can be evaluated.

Langley Research Center, Hampton, Virginia

A free-to-roll (FTR) test technique and test rig make it possible to evaluate both the transonic performance and the wing-drop/rock behavior of a high-strength airplane model in a single wind-tunnel entry. The free-to-roll test technique is a single degree-of-motion method in which the model is free to roll about the longitudinal axis. The rolling motion is observed, recorded, and analyzed to gain insight into wing-drop/rock behavior.

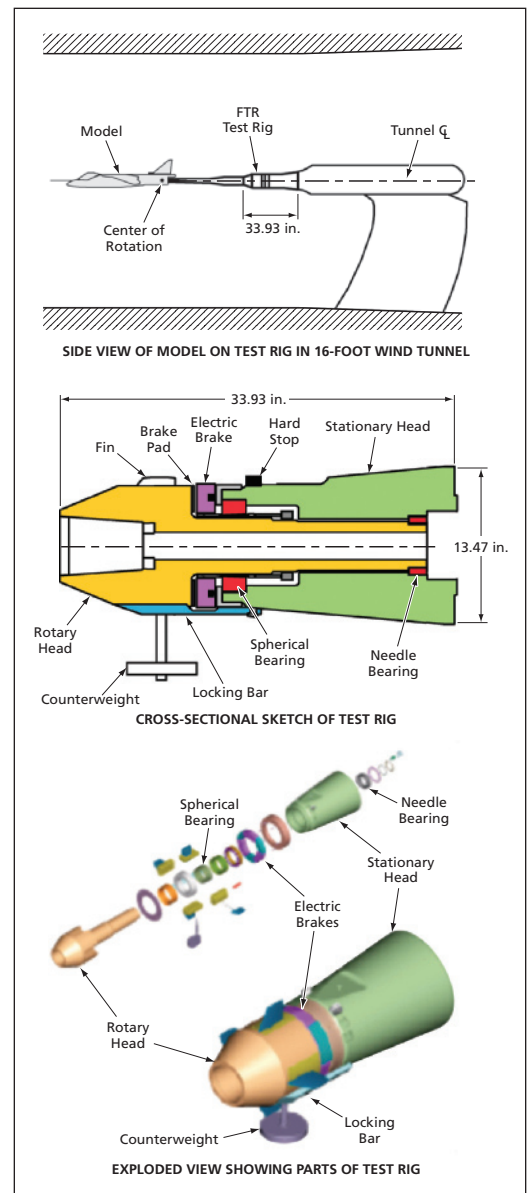
Wing-drop/rock is one of several phenomena symptomatic of abrupt wing stall. FTR testing was developed as part of the NASA/Navy Abrupt Wing Stall Program, which was established for the purposes of understanding and preventing significant unexpected and uncommanded (thus, highly undesirable) lateral-directional motions associated with wing-drop/rock, which have been observed mostly in fighter airplanes under high-subsonic and transonic maneuvering conditions. Before FTR testing became available, wing-rock/drop behavior of high-performance airplanes undergoing development was not recognized until flight testing. FTR testing is a reliable means of detecting, and evaluating design modifications for reducing or preventing, very complex abrupt wing stall phenomena in a ground facility prior to flight testing.

The FTR test rig was designed to replace an older sting attachment butt, such that a model with its force balance and support sting could freely rotate about the longitudinal axis. The rig (see figure) includes a rotary head supported in a stationary head with a forward spherical roller bearing and an aft needle bearing. Rotation is amplified by a set of gears and measured by a shaft-angle resolver; the roll angle can be resolved to within 0.067° at a

rotational speed up to $1,000^\circ/\text{s}$. An assembly of electrically actuated brakes between the rotary and stationary heads can be used to hold the model against a rolling torque at a commanded roll angle. When static testing is required, a locking bar is used to fix the rotating head rigidly to the stationary head. Switching between the static and FTR test modes takes only about 30 minutes. The FTR test rig was originally mounted in a 16-ft ($\approx 4.0\text{-m}$) transonic wind tunnel, but could just as well be adapted to use in any large wind tunnel.

In one series of tests on the FTR rig, static and dynamic characteristics of models of four different fighter airplanes were measured. Two of the models exhibited uncommanded lateral motions; the other two did not. A figure of merit was developed to discern the severity of lateral motions. Using this figure of merit, it was shown that the FTR test technique enabled identification of conditions under which the uncommanded lateral motions occurred. The wind-tunnel conditions thus identified were found to be correlated with flight conditions under which the corresponding full-size airplanes exhibited uncommanded lateral motions.

This work was done by Francis J. Capone, D. Bruce Owens, and Robert M. Hall of Langley Research Center. Further information is contained in a TSP (see page 1). LAR-17153-1



The FTR Test Rig allows free rotation of the airplane model around the centerline. Optionally, brakes can hold the model at a commanded roll angle, or the rig can be locked against rotation for conventional static testing.

Cryogenic Shrouds for Testing Thermal-Insulation Panels

These shrouds enable maintenance of required thermal and mechanical conditions.

Marshall Space Flight Center, Alabama

Cryogenic shrouds have been designed and built for use in thermomechanical testing of samples of thermal-insulation panels on cryogenic vessels. In the original application for which these shrouds were specifically designed, the samples are representative of the large-area thermal-insulation panels on the space-shuttle external tanks that hold liquid hydrogen and liquid oxygen, and the purpose of the testing is to demonstrate the ability of bonded layers in the panels to resist delamination under a combination of applied uniaxial mechanical loads and realistic operational temperatures. Presumably, the shrouds and the tests performed by use of them could be modified to enable similar evaluation of thermomechanical properties of thermal-insulation panels for cryogenic vessels other than the external tanks of the space shuttles.

The shrouds are required to enable maintenance of required temperatures on the inner and outer surfaces of the thermal-insulation-panel samples, to enable visual observation of the outer sur-

faces of the samples, and not to introduce any measurable loads into the panels. For each panel sample, there are two shrouds: one to be mounted on the inner surface (the surface that would be in contact with a tank containing a cryogenic liquid during normal use) and one to be mounted on the outer surface (the surface that would be exposed to ambient air or other warmer environment during normal use). The shrouds for testing specimens of thermal-insulation-panels for the liquid-hydrogen tank are made largely of titanium; the shrouds for testing specimens of thermal-insulation-panels for the liquid-oxygen tank are made largely of an aluminum-lithium alloy.

The specific temperature requirements are the following: The inner shroud must make it possible to maintain a temperature of -321°F (-196°C) [the approximate temperature of liquid nitrogen] or -453°F (about -269°C) [the approximate temperature of liquid helium] on the inner face of the sample. The outer shroud must make it possible

to maintain a temperature between -30 and 0°F (between about -34 and about -18°C) on the outer surface of the sample by blowing a cryogenic gas or missile-grade air along that surface. To enable viewing of the outer surface of the sample during testing, the outer shroud includes a window comprising two layers of poly(methyl methacrylate) with a gap between them to reduce fogging.

To ensure that the shrouds do not introduce any measurable loads into a panel specimen, the shrouds are cushioned on the specimen by seals made of a fluoropolymer-membrane/fabric composite material and are held in place on the specimen by means of symmetrically placed clamps with poly(tetrafluoroethylene) pads. Instrumentation ports for thermocouples and strain gauges used in the tests are incorporated into the shrouds.

This work was done by Jeffrey Norris, Robert Carroll, and Charles Kirch of Lockheed Martin Corp. for Marshall Space Flight Center. Further information is contained in a TSP (see page 1). MFS-32444-1



Optoelectronic System Measures Distances to Multiple Targets

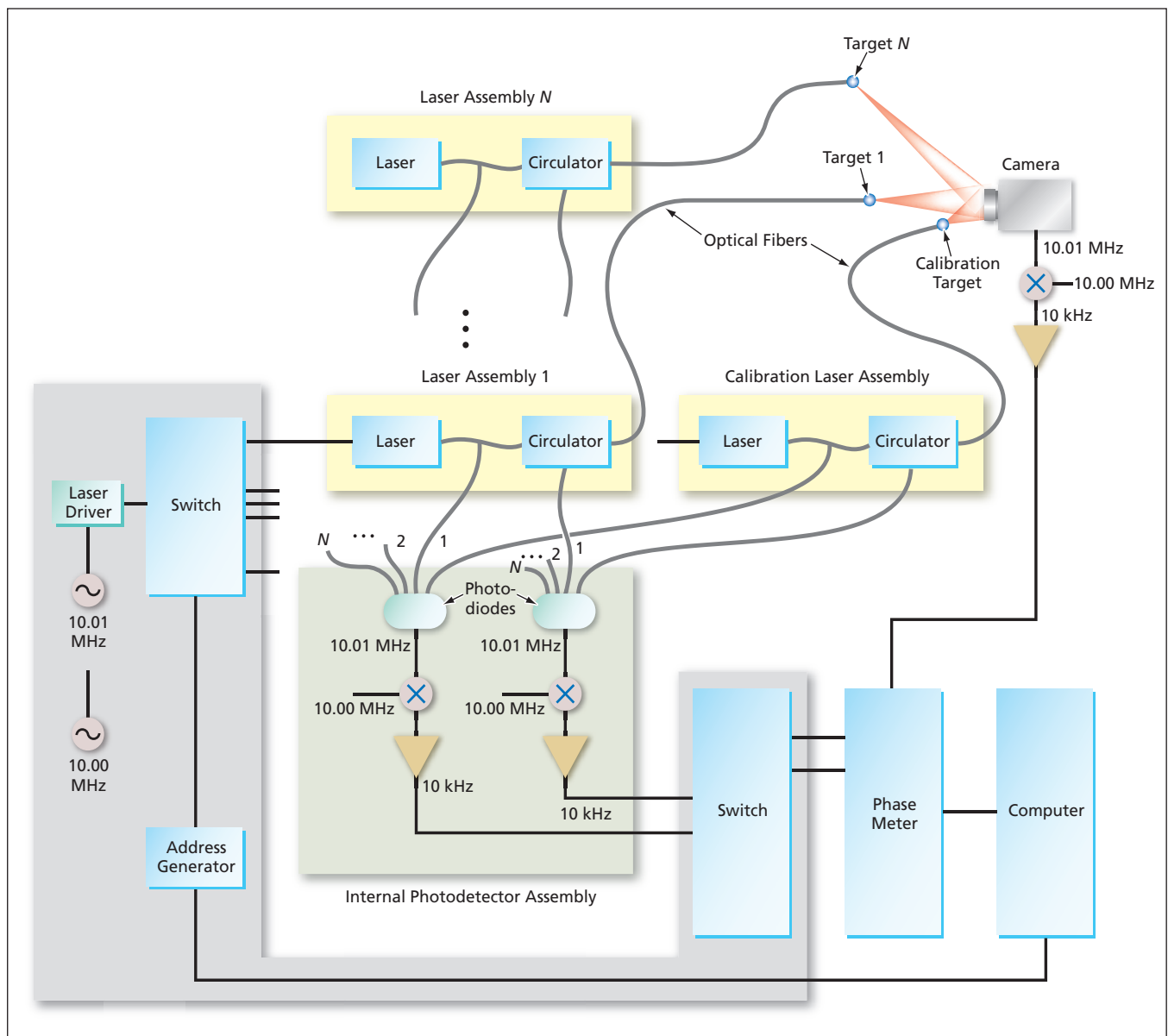
This system operates at an update rate >10 Hz.

NASA's Jet Propulsion Laboratory, Pasadena, California

An optoelectronic metrology apparatus now at the laboratory-prototype stage of development is intended to repeatedly determine distances of as much as several hundred meters, at sub-millimeter accuracy, to multiple targets

in rapid succession. The underlying concept of optoelectronic apparatuses that can measure distances to targets is not new; such apparatuses are commonly used in general surveying and machining. However, until now such ap-

paratuses have been, variously, constrained to (1) a single target or (2) multiple targets with a low update rate and a requirement for some *a priori* knowledge of target geometry. When fully developed, the present apparatus



This Apparatus Includes N Laser Assemblies (of which only the first and N th are shown here), for measuring distances to N targets. The lasers are turned on, one at a time, to illuminate their targets for short intervals in rapid succession to obtain a high update rate.

would enable measurement of distances to more than 50 targets at an update rate >10 Hz, without a requirement for *a priori* knowledge of target geometry.

The apparatus (see figure) includes a laser ranging unit (LRU) that includes an electronic camera (photo receiver), the field of view of which contains all relevant targets. Each target, mounted at a fiducial position on an object of interest, consists of a small lens at the output end of an optical fiber that extends from the object of interest back to the LRU. For each target and its optical fiber, there is a dedicated laser that is used to illuminate the target via the optical fiber. The targets are illuminated, one at a time, with laser light that is modulated at a frequency of 10.01 MHz. The modulated laser light is emitted by the target, from where it returns to the camera (photodetector), where it is detected.

Both the outgoing and incoming 10.01-MHz laser signals are mixed with

a 10-MHz local-oscillator to obtain beat notes at 10 kHz, and the difference between the phases of the beat notes is measured by a phase meter. This phase difference serves as a measure of the total length of the path traveled by light going out through the optical fiber and returning to the camera (photodetector) through free space.

Because the portion of the path length inside the optical fiber is not ordinarily known and can change with temperature, it is also necessary to measure the phase difference associated with this portion and subtract it from the aforementioned overall phase difference to obtain the phase difference proportional to only the free-space path length, which is the distance that one seeks to measure. Therefore, the apparatus includes a photodiode and a circulator that enable measurement of the phase difference associated with propagation from the LRU inside the fiber to the target, reflection from the fiber end,

and propagation back inside the fiber to the LRU. Because this phase difference represents twice the optical path length of the fiber, this phase difference is divided in two before subtraction from the aforementioned total-path-length phase difference.

Radiation-induced changes in the photodetectors in this apparatus can affect the measurements. To enable calibration for the purpose of compensation for these changes, the apparatus includes an additional target at a known short distance, located inside the camera. If the measured distance to this target changes, then the change is applied to the other targets.

This work was done by Carl Christian Liebe, Alexander Abramovici, Randall Bartman, Jacob Chapsky, John Schmalz, Keith Coste, Edward Litty, Raymond Lam, and Sergei Jerebets of Caltech for NASA's Jet Propulsion Laboratory. Further information is contained in a TSP (see page 1). NPO-43240

Tachometers Derived From a Brushless DC Motor

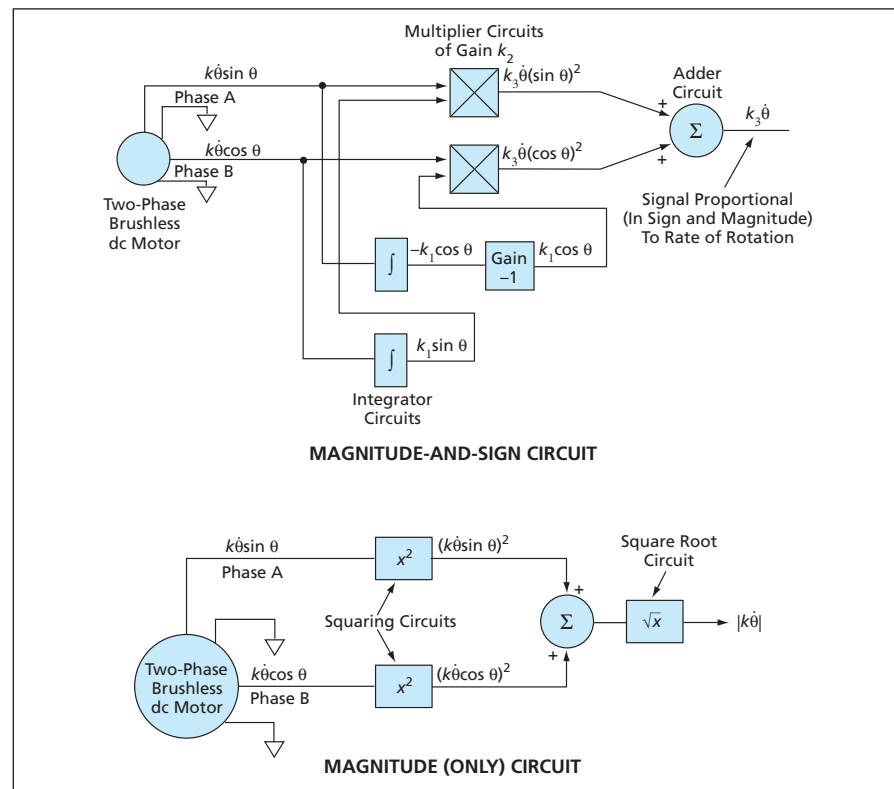
Neither excitation of the motor nor mechanical brushes is necessary.

Marshall Space Flight Center, Alabama

The upper part of the figure illustrates the major functional blocks of a direction-sensitive analog tachometer circuit based on the use of an unexcited two-phase brushless dc motor as a rotation transducer. The primary advantages of this circuit over many older tachometer circuits include the following:

- Its output inherently varies linearly with the rate of rotation of the shaft.
- Unlike some tachometer circuits that rely on differentiation of voltages with respect to time, this circuit relies on integration, which results in signals that are less noisy.
- There is no need for an additional shaft-angle sensor, nor is there any need to supply electrical excitation to a shaft-angle sensor.
- There is no need for mechanical brushes (which tend to act as sources of electrical noise).
- The underlying concept and electrical design are relatively simple.

This circuit processes the back-electromagnetic force (back-emf) outputs of the two motor phases into a voltage directly proportional to the instantaneous rate (sign · magnitude) of rota-



These Analog Tachometer Circuits perform straightforward operations on the back-emf outputs of a brushless dc motor to generate voltages proportional to the rate of rotation of the shaft.

tion of the shaft. The processing in this circuit effects a straightforward combination of mathematical operations leading to a final operation based on the well-known trigonometric identity $(\sin x)^2 + (\cos x)^2 = 1$ for any value of x . The principle of operation of this circuit is closely related to that of the tachometer circuit described in "Tachometer Derived From Brushless Shaft-Angle Resolver" (MFS-28845), *NASA Tech Briefs*, Vol. 19, No. 3 (March 1995), page 39. However, the present circuit is simpler in some respects because there is no need for sinusoidal excitation of shaft-angle-resolver windings.

The two back-emf signals are $k \dot{\theta} \sin \theta$ for phase A and $k \dot{\theta} \cos \theta$ for phase B, where k is a constant that depends on the electromagnetic characteristics of the motor, θ is the instantaneous shaft angle, and the overdot signifies differentiation with respect to time. Note that $\dot{\theta}$ is the quantity that one seeks to measure.

Each back-emf signal is fed to one of two inputs of a multiplier circuit of gain k_2 dedicated to its respective phase. Each of these signals is also integrated with a suitable time constant and gain to obtain a voltage of $k_1 \sin \theta$ for phase A and $-k_1 \cos \theta$ for phase B (where k_1 is a constant that incorpo-

rates the combined effects of the gain and the time constant). The output of the integrator for phase B is inverted to obtain a voltage $k_1 \cos \theta$. Each of these signals is fed to the other input terminal of the multiplier circuit for its respective phase.

The multiplier circuit for phase A thus generates an output signal proportional to both of its inputs; namely $k_3 \theta (\sin \theta)^2$, where $k_3 = k_1 k_2$. In a similar manner, the multiplier circuit for phase B generates an output signal of $k_3 \theta (\cos \theta)^2$. These signals are fed to an adder circuit. By virtue of the identity $(\sin \theta)^2 + (\cos \theta)^2 = 1$, the output of the adder is simply $k_3 \theta$.

The lower part of the figure illustrates the major functional blocks of a direction-insensitive analog tachometer that, except for its lack of directionality, offers the same advantages as does the analog tachometer described above. However, this circuit is conceptually simpler in that it does not contain integrators.

This circuit processes the back-emf outputs of the two motor phases into a voltage directly proportional to magnitude of the instantaneous rate of rotation of the shaft. As in the circuit described above, the processing in this circuit effects a straightforward combination of mathematical operations

leading to a final operation based on the identity $(\sin x)^2 + (\cos x)^2 = 1$ for any value of x .

Further as in the circuit described above, the two back-emf signals are $k \dot{\theta} \sin \theta$ for phase A and $k \dot{\theta} \cos \theta$ for phase B, where k is a constant that depends on the electromagnetic characteristics of the motor. In the present case, the quantity that one seeks to measure is $|\dot{\theta}|$.

Each back-emf signal is fed to a dedicated squaring circuit. The outputs of the squaring circuits for phases A and B are thus proportional to $(\dot{\theta} \sin \theta)^2$ and $(\dot{\theta} \cos \theta)^2$. The outputs of the squaring circuits are fed to an adder. By virtue of the identity $(\sin \theta)^2 + (\cos \theta)^2 = 1$ the output of the adder is proportional to $\dot{\theta}^2$; this output is fed to a square-root circuit to obtain a final output proportional to $|\dot{\theta}|$.

This work was done by David E. Howard and Dennis A. Smith of Marshall Space Flight Center. Further information is contained in a TSP (see page 1).

This invention has been patented by NASA (U.S. Patent No. 6,084,398). Inquiries concerning nonexclusive or exclusive license for its commercial development should be addressed to Sammy Nabors, MSFC Commercialization Assistance Lead, at sammy.a.nabors@nasa.gov. Refer to MFS-31142/3.



Algorithm-Based Fault Tolerance for Numerical Subroutines

A software library implements a new methodology of detecting faults in numerical subroutines, thus enabling application programs that contain the subroutines to recover transparently from single-event upsets. The software library in question is fault-detecting middleware that is wrapped around the numerical subroutines. Conventional serial versions (based on LAPACK and FFTW) and a parallel version (based on ScaLAPACK) exist. The source code of the application program that contains the numerical subroutines is not modified, and the middleware is transparent to the user.

The methodology used is a type of algorithm-based fault tolerance (ABFT). In ABFT, a checksum is computed before a computation and compared with the checksum of the computational result; an error is declared if the difference between the checksums exceeds some threshold. Novel normalization methods are used in the checksum comparison to ensure correct fault detections independent of algorithm inputs. In tests of this software reported in the peer-reviewed literature, this library was shown to enable detection of 99.9 percent of significant faults while generating no false alarms.

This program was written by Michael Turmon, Robert Granat, and John Lou of Caltech for NASA's Jet Propulsion Laboratory.

This software is available for commercial licensing. Please contact Karina Edmonds of the California Institute of Technology at (626) 395-2322. Refer to NPO-42193.

Computational Support for Technology-Investment Decisions

Strategic Assessment of Risk and Technology (START) is a user-friendly computer program that assists human managers in making decisions regarding research-and-development investment portfolios in the presence of uncertainties and of non-technological constraints that include budgetary and time limits, restrictions related to infrastructure, and programmatic and institutional priorities. START facilitates quantitative analysis of technologies, capabilities, missions, scenarios and programs, and thereby enables

the selection and scheduling of value-optimal development efforts. START incorporates features that, variously, perform or support a unique combination of functions, most of which are not systematically performed or supported by prior decision-support software. These functions include the following:

- Optimal portfolio selection using an expected-utility-based assessment of capabilities and technologies;
- Temporal investment recommendations;
- Distinctions between enhancing and enabling capabilities;
- Analysis of partial funding for enhancing capabilities; and
- Sensitivity and uncertainty analysis.

START can run on almost any computing hardware, within Linux and related operating systems that include Mac OS X versions 10.3 and later, and can run in Windows under the Cygwin environment. START can be distributed in binary code form. START calls, as external libraries, several open-source software packages. Output is in Excel (.xls) file format.

This program was written by Virgil Adumitroaie, Hook Hua, William Lincoln, Gary Block, Joseph Mrozinski, Kacie Shelton, Charles Weisbin, Alberto Elfes, and Jeffrey Smith of Caltech for NASA's Jet Propulsion Laboratory. Further information is contained in a TSP (see page 1).

This software is available for commercial licensing. Please contact Karina Edmonds of the California Institute of Technology at (626) 395-2322. Refer to NPO-44800.

DSN Resource Scheduling

TIGRAS is client-side software, which provides tracking-station equipment planning, allocation, and scheduling services to the DSMS (Deep Space Mission System). TIGRAS provides functions for schedulers to coordinate the DSN (Deep Space Network) antenna usage time and to resolve the resource usage conflicts among tracking passes, antenna calibrations, maintenance, and system testing activities. TIGRAS provides a fully integrated multi-pane graphical user interface for all scheduling operations. This is a great improvement over the legacy VAX VMS command line user interface.

TIGRAS has the capability to handle all DSN resource scheduling aspects from long-range to real time. TIGRAS assists

NASA mission operations for DSN tracking of station equipment resource request processes from long-range load forecasts (ten years or longer), to mid-range, short-range, and real-time (less than one week) emergency tracking plan changes. TIGRAS can be operated by NASA mission operations worldwide to make schedule requests for the DSN station equipment.

This program was written by Yeou-Fang Wang and John Baldwin of Caltech for NASA's Jet Propulsion Laboratory.

This software is available for commercial licensing. Please contact Karina Edmonds of the California Institute of Technology at (626) 395-2322. Refer to NPO-43771.

Distributed Operations Planning

Maestro software provides a secure and distributed mission planning system for long-term missions in general, and the Mars Exploration Rover Mission (MER) specifically. Maestro, the successor to the Science Activity Planner, has a heavy emphasis on portability and distributed operations, and requires no data replication or expensive hardware, instead relying on a set of services functioning on JPL institutional servers.

Maestro works on most current computers with network connections, including laptops. When browsing down-link data from a spacecraft, Maestro functions similarly to being on a Web browser. After authenticating the user, it connects to a database server to query an index of data products. It then contacts a Web server to download and display the actual data products. The software also includes collaboration support based upon a highly reliable messaging system. Modifications made to targets in one instance are quickly and securely transmitted to other instances of Maestro.

The back end that has been developed for Maestro could benefit many future missions by reducing the cost of centralized operations system architecture.

This program was written by Jason Fox, Jeffrey Norris, Mark Powell, Kenneth Rabe, and Khawaja Shams of Caltech for NASA's Jet Propulsion Laboratory.

This software is available for commercial licensing. Please contact Karina Edmonds of the California Institute of Technology at (626) 395-2322. Refer to NPO-43278.



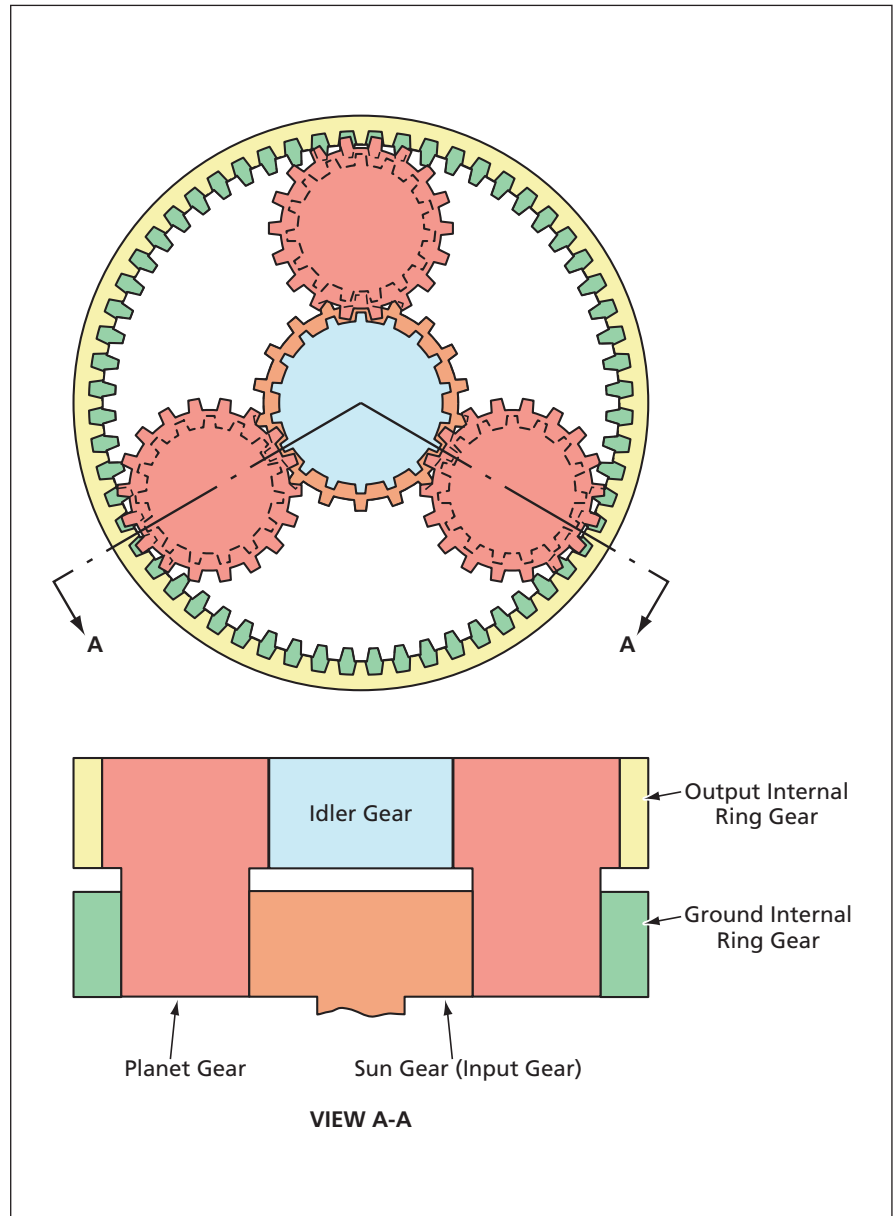
Phase-Oriented Gear Systems

Larger mechanical advantages can be realized in smaller packages.

Goddard Space Flight Center, Greenbelt, Maryland

Phase-oriented gear systems are differential planetary transmissions in which each planet gear has two sets of unequal numbers of teeth indexed at prescribed relative angles (phases). The figure illustrates an application of the phase-oriented gearing concept to a relatively simple speed-reducing differential planetary transmission that includes a sun gear, an idler gear, three identical planet gears, a ground internal ring gear, and an output internal ring gear. Typically, the ground internal ring gear and output internal ring gear have different numbers of teeth, giving rise to a progressive and periodic phase shift between the corresponding pairs of teeth engaged by each successive planet gear. To accommodate this phase shift, it is necessary to introduce a compensating phase shift between the ground-gear-engaging and output-gear-engaging sections of each planet gear. This is done by individually orienting each planet gear.

Each planet gear consists of a top (output-gear-engaging) part and a bottom (ground-gear-engaging) part that are coaxially joined into a unit. Typically, the numbers of teeth in the top and bottom parts differ by one, (but could differ by more than one). Typically, the teeth on the bottom part are indexed with those on the top part such that at least one tooth on the bottom part lies at the same angular position as does one tooth on the top part; in other words, these two teeth are in phase with each other. The next tooth on the top part is slightly out of phase with the nearest corresponding tooth on the bottom part. Proceeding circumferentially around the planet gear, this phase difference increases linearly, tooth-by-tooth, until the total phase change reaches 360° upon completing one full rotation. Depending on the specific numbers of teeth, such an arrangement could offer many tooth-phasing possibilities, making it possible to include various numbers of appropriately phased (oriented) planet gears. This is advantageous because in some applications, it is desirable to increase numbers of planet



Different Numbers of Teeth on the upper and lower part of each planet gear are used to accommodate the phase differences occasioned by the use of different numbers of teeth on the ground and output gears.

gears in order to make more teeth share the total load, thereby reducing loads on individual teeth.

The phase-oriented gearing concept admits of so many variations that is not possible to describe or even to merely

list them within the space available for this article. In general, it can be said that the numbers of teeth and the angles can be chosen to achieve desired speed ratios and other design goals. The phase-oriented gearing concept can be

implemented in conjunction with other advanced planetary-gearing concepts, including those of carrierless and gear-bearing transmission types described in several *NASA Tech Briefs* articles in recent years. Relative to prior differential planetary transmissions, phase-oriented gear systems offer advantages of simplicity, ruggedness, strength, and smooth-

ness of operation. Moreover, for a typical speed-reducing transmission, phase-oriented gearing makes it possible to obtain unprecedentedly large mechanical advantage in a compact package — in effect, what previously would have been characterized as two-stage performance in the space previously occupied by a one-stage package.

This work was done by John M. Vranish of Goddard Space Flight Center.

This invention is owned by NASA, and a patent application has been filed. Inquiries concerning nonexclusive or exclusive license for its commercial development should be addressed to the Patent Counsel, Goddard Space Flight Center, (301) 286-7351. Refer to GSC-14790-1.



Freeze Tape Casting of Functionally Graded Porous Ceramics

Pore structures can be tailored in ways heretofore impossible.

John H. Glenn Research Center, Cleveland, Ohio

Freeze tape casting is a means of making preforms of ceramic sheets that, upon subsequent completion of fabrication processing, can have anisotropic and/or functionally graded properties that notably include aligned and graded porosity. Freeze tape casting was developed to enable optimization of the microstructures of porous ceramic components for use as solid oxide electrodes in fuel cells: Through alignment and grading of pores, one can tailor surface areas and diffusion channels for flows of gas and liquid species involved in fuel-cell reactions. Freeze tape casting offers similar benefits for fabrication of optimally porous ceramics for use as catalysts, gas sensors, and filters.

Freeze tape casting includes, and goes beyond, traditional tape casting, in which an aqueous ceramic slip (ceramic and/or ceramic precursor particles suspended in water) is cast onto a poly(ethylene terephthalate) or poly(tetrafluoroethylene) carrier film by use of a doctor-blade assembly. The slip may also

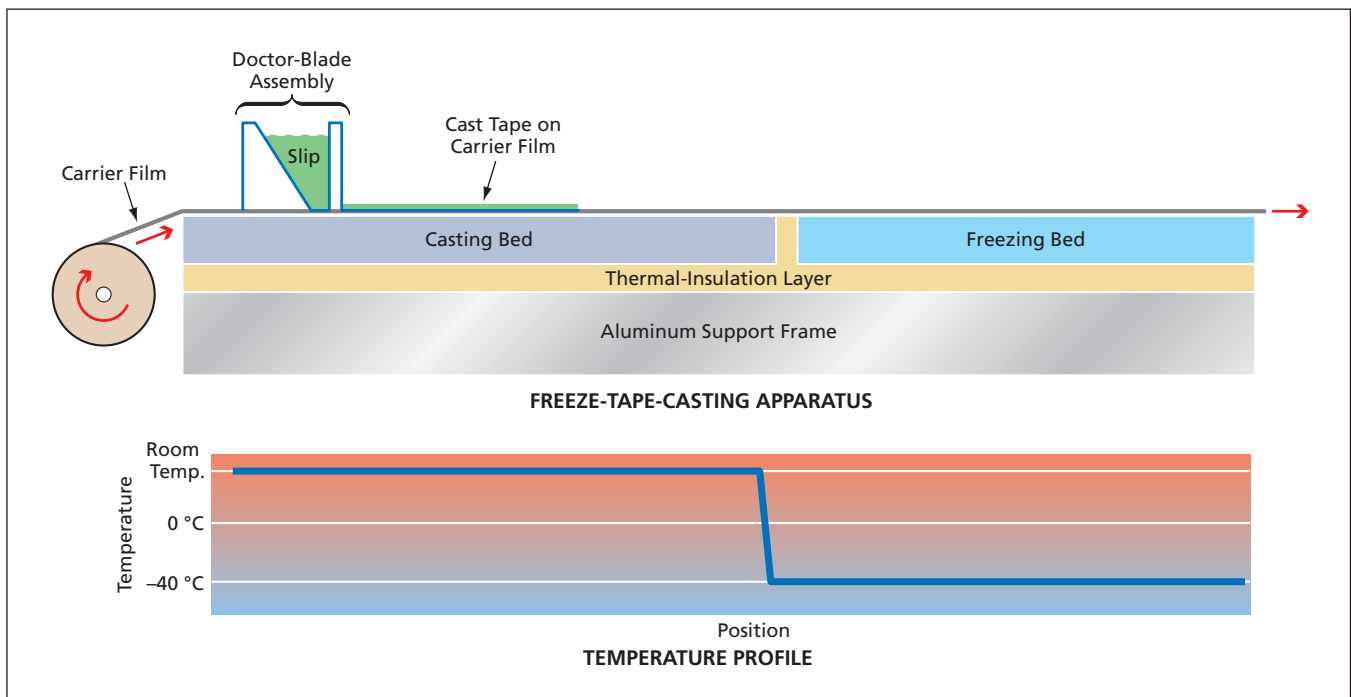
contain one or more organic solvent(s) plus a significant quantity of organic binders that make the tape strong and flexible after evaporation of the solvent(s). Traditional tape casting has been used to make ceramic sheets, for electronic and structural applications, ranging in thickness from 5 μm to 1,000 μm . Freeze tape casting expands this range to greater than 3 mm, thus eliminating the need for lamination steps in traditional processing.

An apparatus for freeze tape casting (see figure) is basically a traditional tape-casting apparatus augmented with a freezing bed. By use of the freezing bed, the water in the slip is frozen, from the bottom up through the thickness, immediately after the tape has been cast. For fabricating a porous ceramic, the freezing affords several advantages over traditional tape casting:

- In traditional tape casting, the water and any organic solvents are allowed to evaporate slowly before the tape is sintered to form the final ceramic. The evapora-

tion can cause or be accompanied by undesired compositional and physical changes, including settling of particles out of suspension and density gradients. The freezing prevents such changes.

- Water alone or high melting point organic solvents (including benzene, cyclohexane, tertiary butyl alcohol, and camphene), can become formed into channels or other unique pore structures when directionally solidified. The channels or other pore structures can be tailored to some extent through control of the rate of freezing and/or the addition of such freezing additives as glycerol, glycols, anti-freeze proteins, and/or alcohols.
- Porosity can also be tailored through choice of the concentration of suspended ceramic particles: typically, freeze-tape-cast ceramics contain open pore structures when the slips contain less than 45 volume percent of ceramic and/or metallic solids.
- In freeze tape casting, the solids loading can be made as low as 5 volume percent



In **Freeze Tape Casting**, a slip is cast into a tape as in traditional tape casting, but then, unlike traditional tape casting, the water and any other solvents in the tape are frozen. The frozen tape is then freeze-dried before sintering. (Temperature profile is indicated for an aqueous system)

to obtain exceptionally high porosity.

After casting and freezing, the frozen tape is diced into sections for freeze-drying, in which the water and any other solvents are removed by sublimation. Because, in sublimation, the solidified solvents are transformed into gases without passing through intermediate liquid phases, there are no capillary forces like those associated with liquid-to-vapor transitions that occur

during drying in traditional tape casting. Because of the absence of capillary forces, the changes in the dimensions of microstructures and in the overall thickness of the tape are negligible and hence processing is simplified with the absence of cracks and other drying defects notable in traditional tapes. After freeze-drying, the sections of tape are cut into the desired shape, then sintered.

This work was done by Stephen W. Sofie of QSS Group, Inc. for Glenn Research Center. Further information is contained in a TSP (see page 1).

Inquiries concerning rights for the commercial use of this invention should be addressed to NASA Glenn Research Center, Innovative Partnerships Office, Attn: Steve Fedor, Mail Stop 4-8, 21000 Brookpark Road, Cleveland, Ohio 44135. Refer to LEW-17628-1.

Electrophoretic Deposition on Porous Non-Conductors

EPD is simplified and made more widely applicable.

John H. Glenn Research Center, Cleveland, Ohio

A method of electrophoretic deposition (EPD) on substrates that are porous and electrically non-conductive has been invented. Heretofore, in order to perform an EPD, it has been necessary to either (1) use a substrate material that is inherently electrically conductive or (2) subject a non-conductive substrate to a thermal and/or chemical treatment to render it conductive.

In the present method, instead of relying on the electrical conductivity of the substrate, one ensures that the substrate is porous enough that when it is immersed in an EPD bath, the solvent penetrates throughout the thickness, thereby forming quasi-conductive paths through the substrate. By making it unnecessary to use a conductive substrate, this method simplifies the overall EPD process and makes new applications possible. The method is expected to be especially beneficial in enabling deposition of layers of ceramic and/or metal for chemical and electrochemical devices, notably including solid oxide fuel cells.

In the initial application for which this method was invented, there is a requirement to fabricate unitary anode/solid electrolyte structures for solid oxide fuel cells, each such structure comprising the following:

- A porous cermet anode layer made of nickel and yttria-stabilized zirconia (YSZ) and
- A solid electrolyte in the form a thin dense layer of YSZ.

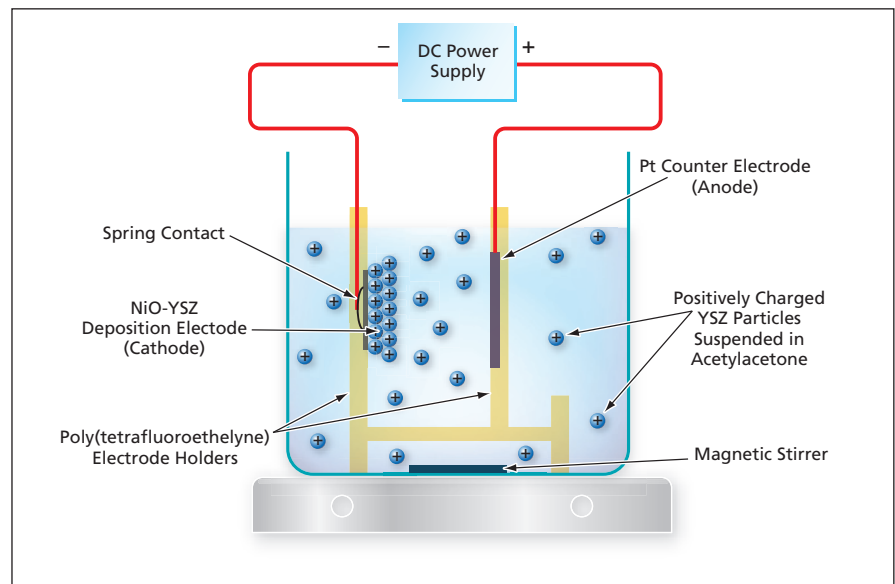
The starting material for fabricating the structure is a porous layer consisting mostly of pellets of a composite of NiO and YSZ. The dense layer of YSZ is deposited on the NiO-YSZ composite later by means of EPD according to the present method, then the resulting

(NiO-YSZ)/YSZ structure is sintered. The final fabrication step takes place after the sintered structure has been placed in a fuel cell: The reducing atmosphere maintained on the anode side of the fuel cell during testing reduces the NiO to metallic Ni, thereby creating the desired Ni anode having the porosity needed for transport of reactant and product gases.

The figure depicts the apparatus used in experiments to develop and demonstrate the present EPD method. The apparatus included a reservoir containing acetylacetone (as a nominally nonaqueous solvent). YSZ powder was stably suspended in the solvent by electrostatic repulsion, and YSZ particles were replenished to the depositing electrode by use of a magnetic stirrer. The YSZ particles acquired positive surface electric

charges in a manner similar to that of surface charging in an aqueous medium. This charging has been conjectured to be a consequence of the presence of residual water in the acetylacetone. Regardless of the exact physical mechanism, the charging was fortuitous in that it contributed to the desired electrophoretic effect.

The NiO-YSZ deposition substrate was mounted on a stationary poly(tetrafluoroethylene) electrode holder and connected via a spring contact to the negative side of a DC power supply so that it became a deposition electrode (cathode). A platinum counter electrode was mounted on a movable poly(tetrafluoroethylene) electrode holder and connected to the positive side of the power supply, so that it became an anode. For most experimental



Particles of YSZ Were Deposited on an NiO-YSZ substrate in this experimental EPD apparatus.

depositions, the distance between the electrodes was kept at 10 mm. The depositions were carried out at various constant applied voltages ranging from 50 to 300 V for periods of 30 s to 5 min. During each deposition, the force of the applied electric field on suspended YSZ particles caused these particles to migrate towards the cathode and even-

tually deposit. A solid-oxide fuel cell containing an anode/solid-electrolyte structure fabricated in part by this method exhibited an areal power density of 611 W/cm² in operation at a temperature of 800 °C.

This work was done by Charles Compson, Laxmidhar Besra, and Meilin Liu of Georgia Institute of Technology for Glenn Research

Center. Further information is contained in a TSP (see page 1).

Inquiries concerning rights for the commercial use of this invention should be addressed to NASA Glenn Research Center, Innovative Partnerships Office, Attn: Steve Fedor, Mail Stop 4-8, 21000 Brookpark Road, Cleveland, Ohio 44135. Refer to LEW-18009-1.



Two Devices for Removing Sludge From Bioreactor Wastewater

These devices can operate continuously and are self-cleaning.

Lyndon B. Johnson Space Center, Houston, Texas

Two devices — a magnetic separator and a special filter denoted a self-regenerating separator (SRS) — have been developed for separating sludge from the stream of wastewater from a bioreactor. These devices were originally intended for use in microgravity, but have also been demonstrated to function in normal Earth gravity.

The magnetic separator (see Figure 1) includes a thin-walled nonmagnetic, stainless-steel cylindrical drum that rotates within a cylindrical housing. The wastewater enters the separator

through a recirculation inlet, and about 80 percent of the wastewater flow leaves through a recirculation outlet. Inside the drum, a magnet holder positions strong permanent magnets stationary and, except near a recirculation outlet, close to the inner drum surface. To enable magnetic separation, magnetite (a ferromagnetic and magnetically soft iron oxide) powder is mixed into the bioreactor wastewater. The magnetite becomes incorporated into the sludge by condensation, onto the

powder particles, of microbe flocks that constitute the sludge. As a result, the magnets inside the drum magnetically attract the sludge onto the outer surface of the drum.

As the drum rotates, it carries the attracted sludge to the recirculation outlet; the decrease in the magnetic field at this location releases the sludge from the drum, making it possible for the sludge to be flushed out by the recirculation-outlet flow. A poly(tetrafluoroethylene) scraper aids in removing any remnants of sludge that may still stick to the drum. An effluent outlet is positioned as far as possible from the recirculation ports in order to provide the longest possible separation path. The effluent flow amounts to about 20 percent of the inlet flow. The flows of sludge and effluent are controlled by use of a recirculation pump and an effluent pump, respectively.

The SRS (see Figure 2) includes two concentric tubes with relatively coarse filtering material (pipe cleaners) in the annular space between them. The wastewater is recirculated through the inner tube. Through an axial slot in the inner tube, a portion of the flow is diverted into the annular space between the tubes. This portion of the flow becomes filtered in the annular space and is drawn off as effluent through an axial slot in the outer tube on the side opposite that of the slot in the inner tube.

Eventually, any conventional filter becomes clogged and thereby loses hydraulic capacity and must be replaced. An ideal filter would have to continuously clean itself so as not to impede the flow of the filtrate. The SRS acts as such an ideal or nearly ideal filter because of the self-regenerating aspect of its operation:

- Initially, sludge builds up quickly in the pipe-cleaner flow field, where the sludge thus trapped serves as a fine filter medium for incoming sludge particles. As more sludge builds up toward the interior of the inner tube, it is ex-

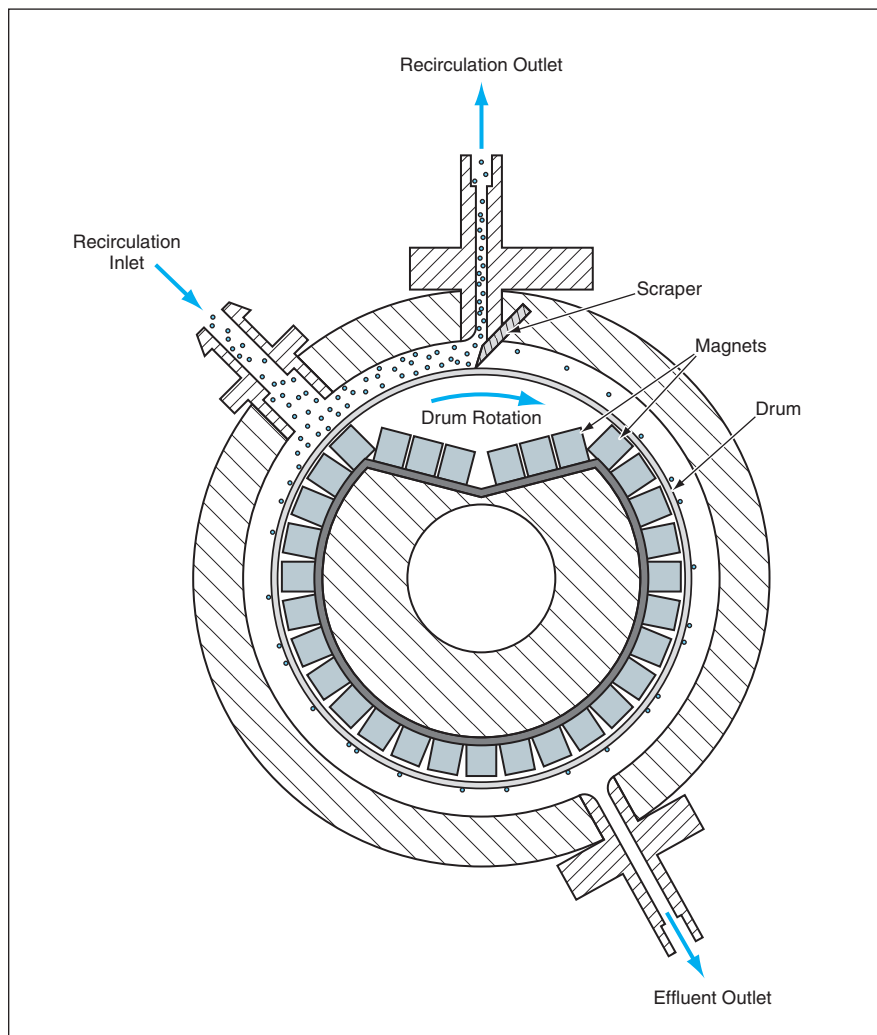


Figure 1. The Magnetic Separator rapidly separates magnetic sludge from wastewater.

posed to the fast recirculation flow, which washes away newly settled sludge. A dynamic equilibrium is quickly reached between the deposition and removal of sludge.

- Unlike what would happen in a conventional filter, the buildup of sludge in the pipe-cleaner flow field does not continue indefinitely until excessive clogging occurs. Instead, the SRS design utilizes the fact that sludge is a living organism that digests its own dead parts stagnating in the pipe-cleaner flow

field. The digestion process continuously opens up new filter pores that make it possible for water to continue to flow. This process gives rise to a second dynamic equilibrium — between clogging and the generation of new flow paths in the pipe-cleaner flow field.

Only the first pipe cleaner is needed as a filter element; the other pipe cleaners are needed only for support of the tubes in their coaxial alignment. Prior to testing, it was expected that sludge would slowly migrate through the pipe-cleaner

flow field and reach the effluent port, where it would reduce the quality of the filtrate. Instead, it was found that the sludge remained stationary at the first pipe cleaner and no migration was observed, even after two weeks of operation.

This work was done by Shivaun Archer, G. Duncan Hitchens, Harry Jabs, Jennifer Cross, Michelle Pilkinton, and Michael Taylor of Lynntech, Inc. for Johnson Space Center. For further information, contact the Johnson Innovative Partnerships Office at (281) 483-3809. Refer to MSC-23293

Portable Unit for Metabolic Analysis

Respiratory signals can be temporally resolved within respiratory cycles.

John H. Glenn Research Center, Cleveland, Ohio

The Portable Unit for Metabolic Analysis (PUMA) is an instrument that measures several quantities indicative of human metabolic function. Specifically, this instrument makes time-resolved measurements of temperature, pressure, flow, and the partial pressures of oxygen and carbon dioxide in breath during both inhalation and exhalation.

Portable instruments for measuring these quantities have been commercially available, but the response times of those instruments are too long to enable temporal resolution of phenomena on the time scales of human respiration cycles. In contrast, the response time of the PUMA is significantly shorter than characteristic times of human respiration phenomena, making it possible to analyze varying metabolic parameters, not only on sequential breath cycles but also at successive phases of inhalation and exhalation within the same breath cycle.

In operation, the PUMA is positioned to sample breath near the subject's mouth. Commercial off-the-shelf sensors

are used for three of the measurements: a miniature pressure transducer for pressure, a thermistor for temperature, and an ultrasonic sensor for flow. Sensors developed at Glenn Research Center are used for measuring the partial pressures of oxygen and carbon dioxide:

- The carbon dioxide sensor exploits the relatively strong absorption of infrared light by carbon dioxide. Light from an infrared source passes through the stream of inhaled or exhaled gas and is focused on an infrared-sensitive photodetector.
- The oxygen sensor exploits the effect of oxygen in quenching the fluorescence of ruthenium-doped organic molecules in a dye on the tip of an optical fiber. A blue laser diode is used to excite the fluorescence, and the optical fiber carries the fluorescent light to a photodiode, the temporal variation of the output of which bears a known relationship with the rate of quenching of fluorescence and, hence, with the partial pressure of oxygen.

The outputs of the sensors are digitized, preprocessed by a small onboard computer, and then sent wirelessly to a desktop computer, where the collected data are analyzed and displayed. In addition to the raw data on temperature, pressure, flow, and mole fractions of oxygen and carbon dioxide, the display can include volumetric oxygen consumption, volumetric carbon dioxide production, respiratory equivalent ratio, and volumetric flow rate of exhaled gas.

This work was done by Daniel L. Dietrich, Nancy D. Piltch, Mark E. Lewis, Jeffrey R. Juergens, Michael J. Lichter, Peter M. Struk, and Dale M. Diedrick of Glenn Research Center; Russell W. Valentine of Case Western Reserve University; and Richard D. Pettigrew of the National Center for Microgravity Research.

Inquiries concerning rights for the commercial use of this invention should be addressed to NASA Glenn Research Center, Innovative Partnerships Office, Attn: Steve Fedor, Mail Stop 4-8, 21000 Brookpark Road, Cleveland, Ohio 44135. Refer to LEW-17945-1.



Flash Diffusivity Technique Applied to Individual Fibers

Inversion of spatially and temporally resolved temperature measurements yields thermal-diffusivity maps.

Lyndon B. Johnson Space Center, Houston, Texas

A variant of the flash diffusivity technique has been devised for determining the thermal diffusivities, and thus the thermal conductivities, of individual aligned fibers. The technique is intended especially for application to nanocomposite fibers, made from narrower fibers of polyphenylene benzobisthiazole (PBZT) and carbon nanotubes. These highly aligned nanocomposite fibers could exploit the high thermal conductivities of carbon nanotubes for thermal-management applications.

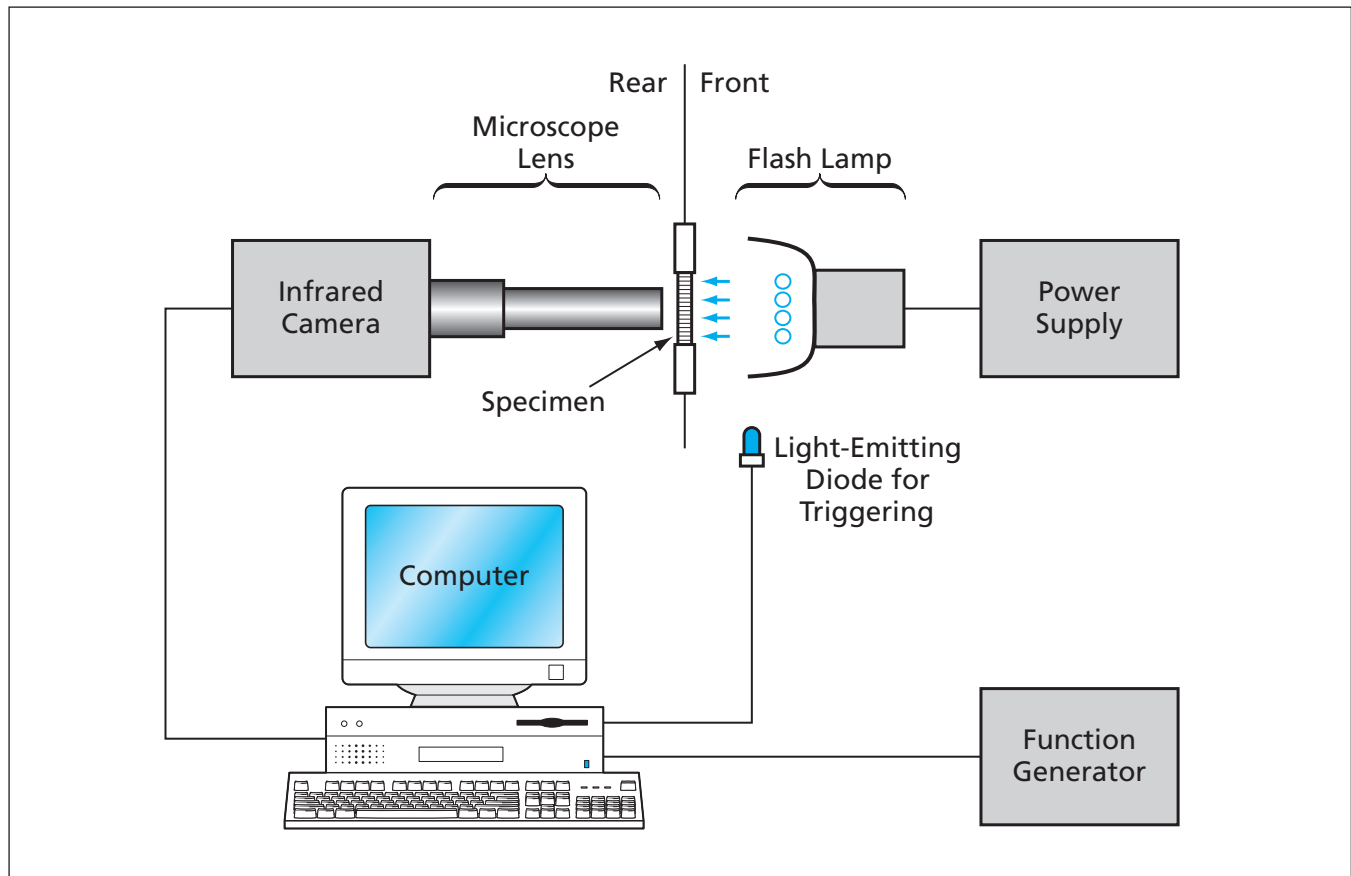
In the flash diffusivity technique as practiced heretofore, one or more heat pulse(s) is (are) applied to the front face of a plate or disk material specimen and the resulting time-varying temperature on the rear face is measured. Usually, the

heat pulse is generated by use of a xenon flash lamp, and the variation of temperature on the rear face is measured by use of an infrared detector. The flash energy is made large enough to produce a usefully high temperature rise on the rear face, but not so large as to significantly alter the specimen material. Once the measurement has been completed, the thermal diffusivity of the specimen is computed from the thickness of the specimen and the time dependence of the temperature variation on the rear face.

Heretofore, the infrared detector used in the flash diffusivity technique has been a single-point detector, which responds to a spatial average of the thermal radiation from the rear specimen surface. Such a detector cannot distin-

guish among regions of differing diffusivity within the specimen. Moreover, two basic assumptions of the thermal-diffusivity technique as practiced heretofore are that the specimen is homogeneous and that heat flows one-dimensionally from the front to the rear face. These assumptions are not valid for an inhomogeneous (composite) material.

In the present variant of the flash diffusivity technique, one uses an infrared electronic camera fitted with a microscope lens to record the spatial as well as the temporal variations in thermal radiation emitted from the rear face of the specimen (see figure). In the recorded image of a composite-material specimen, it is possible to distinguish between



An Infrared Camera With Microscope Lens measures the spatial as well as temporal variations of temperature on the rear face of a specimen that has been flash-heated on its front face.

individual fibers, or between a fiber and the surrounding matrix material. Hence, it is possible to measure the rear-face temperature variations of individual fibers. These variations can be correlated with predictions of a computational model of heat transfer in the composite specimen to obtain a diffusivity map of the specimen.

The technique was demonstrated on a specimen containing pure PBZT fibers, one nanocomposite PBZT/carbon-nanotube fiber, and one copper

fiber mounted longitudinally in an epoxy matrix. The copper fiber, having known thermal conductivity, was included for qualitative comparison. The temperature transients of the pure PBZT fibers were not distinguishable from that of the matrix, and the thermal diffusivity of the matrix and PBZT fibers was found to be $0.0032 \text{ cm}^2/\text{s}$. The thermal diffusivity of the PBZT/carbon-nanotube composite fiber was found to be $0.049 \text{ cm}^2/\text{s}$; the true bulk diffusivity of the PBZT/car-

bon-nanotube composite could be higher than the value computed from the measurements because the heat-transfer model used in the computations does not account for thermal coupling between the fibers and the matrix.

This work was done by Brian Mayeaux, Leonard Yowell of Johnson Space Center, and Hsin Wang of Oak Ridge National Laboratory. For further information, contact the Johnson Innovative Partnerships Office at (281) 483-3809. MSC-23609

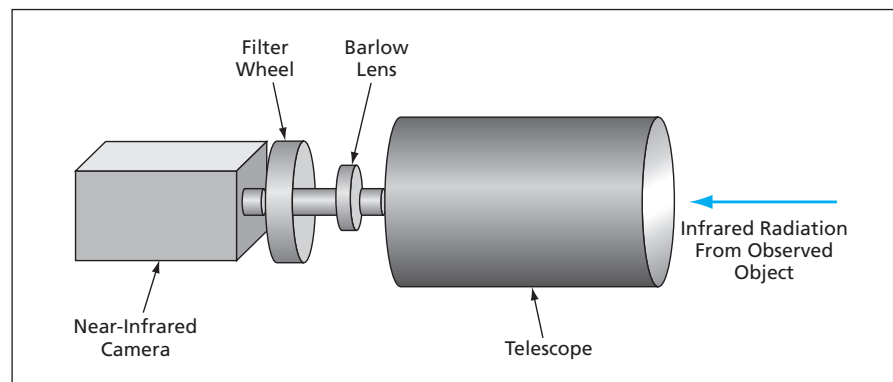
System for Thermal Imaging of Hot Moving Objects

This advanced ratio-intensity thermography system has numerous potential uses.

Langley Research Center, Hampton, Virginia

The High Altitude/Re-Entry Vehicle Infrared Imaging (HARVII) system is a portable instrumentation system for tracking and thermal imaging of a possibly distant and moving object. The HARVII is designed specifically for measuring the changing temperature distribution on a space shuttle as it reenters the atmosphere. The HARVII system or other systems based on the design of the HARVII system could also be used for such purposes as determining temperature distributions in fires, on volcanoes, and on surfaces of hot models in wind tunnels. In yet another potential application, the HARVII or a similar system would be used to infer atmospheric pollution levels from images of the Sun acquired at multiple wavelengths over regions of interest.

The HARVII system includes the Ratio Intensity Thermography System (RITS) and a tracking subsystem that keeps the RITS aimed at the moving object of interest. The subsystem of primary interest here is the RITS (see figure), which acquires and digitizes images of the same scene at different wavelengths in rapid succession. Assuming that the time interval between successive measurements is short enough that temperatures do not change appreciably, the digitized image data at the different wavelengths are processed to extract temperatures according to the principle of ratio-intensity thermography: The temperature at a given location in a scene is inferred from the ratios between or among intensities of infrared radiation from that location at two or more wavelengths. This principle, based on the Stefan-Boltzmann equation for



The RITS Acquires Images at Multiple Wavelengths in rapid succession by means of synchronized operation of a filter wheel and near-infrared camera operating at a frame rate of 30 Hz. The design and mode of operation of this system are such that if two wavelengths are used, then a total of 15 pairs of complete images is acquired during 1 second.

the intensity of electromagnetic radiation as a function of wavelength and temperature, is valid as long as the observed body is a gray or black body and there is minimal atmospheric absorption of radiation.

In this particular variant of ratio-intensity thermography, the wavelengths are chosen to be in the near infrared part of the spectrum and are selected to minimize effects of atmospheric absorption. A nearly ideal pair of wavelengths for minimizing effects of atmospheric absorption would be 1.3 and $1.69 \mu\text{m}$. An additional advantage of this choice of wavelengths is that conventional, high-quality, commercial optics work well at wavelengths below about $2 \mu\text{m}$; if longer wavelengths were chosen, it would be necessary to design and build special infrared optical components.

In practice, it was necessary to choose $1.55 \mu\text{m}$ as the longer of the two wavelengths because the infrared camera

available at the time of development of the RITS was found not to be usable out to $1.69 \mu\text{m}$. In addition, the pass bands of the filters used to select these observation wavelengths were required to be 10 to 20 nm wide in order to enable the acquisition of sufficiently strong signals. The finite widths of these pass bands contribute to variations of atmospheric effects at different water-vapor levels. The use of three or more wavelengths could enable almost complete correction for these effects. Alternately, if one continued to use two wavelengths, then corrections could be derived from measurements made by a spectrometer aimed at the Sun.

This work was done by Leonard Weinstein and Jason Hundley of Langley Research Center. For more information, download the Technical Support Package (free white paper) at www.techbriefs.com/tsp under the Physical Sciences category. LAR-16385-1

Large Solar-Rejection Filter

This lightweight filter comprises a multilayer spectral coating on a flexible membrane.

NASA's Jet Propulsion Laboratory, Pasadena, California

An optical filter consisting of a multilayer spectral coating on a flexible membrane has been designed to be placed in front of the 200-in. (5.08-m) Hale telescope on Mt. Palomar. The filter is intended to protect the telescope against solar radiant flux and limit solar heating of the interior of the telescope dome while transmitting light at the 1,064-nm wavelength of the Mars Laser Communication Demonstration.

For supporting a multilayer spectral coating in this application, the flexible membrane was chosen as a lightweight, less-expensive alternative to a conventional thick optical-glass substrate. Multilayer spectral coatings have been used for decades, and membranes have more recently come into use as substrates for mirrors. However, until now, there have been few (if any) published instances of

multilayer coating of membranes to form lightweight solar-rejection/narrow-band-pass filters.

The main problem to be solved in designing the present filter was to satisfy both (1) the need for a large number (hundreds in a typical first approximation) of coating layers needed to obtain the desired broad-band-solar-rejection/narrow-band-pass spectral characteristic and (2) the need to limit the number of layers to no more than the maximum (≈ 60) that the membrane could support. The solution is a design of fewer than 50 layers having the following features:

- The front surface of the membrane is coated with 25 dielectric layers alternating between higher and lower indices of refraction. These layers are designed to efficiently reflect the visible and near-infrared (wavelengths up to

1.0 μm) light in which the Sun predominantly radiates.

- The back surface of the membrane is coated with very thin layers of copper and silicon chosen to reject the remainder of the spectrum.
- Multiple dielectric layers stacks are deposited on what would otherwise be the exposed opposite outer surfaces of the aforementioned layers. The materials and thicknesses of these layers are chosen to induce the desired narrow passband, centered at 1,064 nm, in the broad-band-reject spectrum of the silicon and copper layers.

This work was done by William Roberts of Caltech, David Sheikh of Surface Optics Corporation, and Brian Patrick of SRS Corporation for NASA's Jet Propulsion Laboratory. For more information, contact taoffice@jpl.nasa.gov NPO-41942

Improved Readout Scheme for SQUID-Based Thermometry

Flux-unit-counting ambiguities would be eliminated.

NASA's Jet Propulsion Laboratory, Pasadena, California

An improved readout scheme has been proposed for high-resolution thermometers, (HRTs) based on the use of superconducting quantum interference devices (SQUIDs) to measure temperature-dependent magnetic susceptibilities. The proposed scheme would eliminate counting ambiguities that arise in the conventional scheme, while maintaining the superior magnetic-flux sensitivity of the conventional scheme. The proposed scheme is expected to be especially beneficial for HRT-based temperature control of multiplexed SQUID-based bolometer sensor arrays.

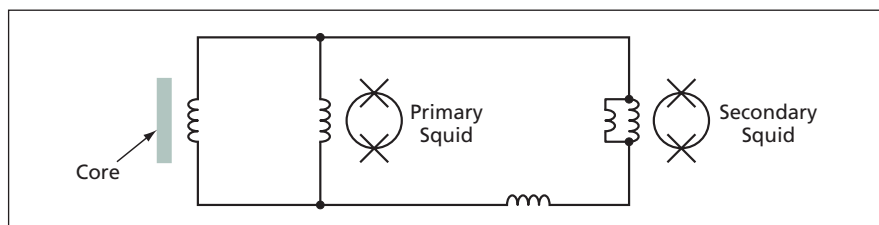
SQUID-based HRTs have become standard for measuring and controlling

temperatures in the sub-nano-Kelvin temperature range in a broad range of low-temperature scientific and engineering applications. A typical SQUID-based HRT that utilizes the conventional scheme includes a coil wound on a core made of a material that has temperature-dependent magnetic susceptibility in the temperature range of interest. The core and the coil are placed in a DC magnetic field provided either by a permanent magnet or as magnetic flux inside a superconducting outer wall. The aforementioned coil is connected to an input coil of a SQUID. Changes in temperature lead to changes in the susceptibility of the core

and to changes in the magnetic flux detected by the SQUID.

The SQUID readout instrumentation is capable of measuring magnetic-flux changes that correspond to temperature changes down to a noise limit ≈ 0.1 nK/Hz^{1/2}. When the flux exceeds a few fundamental flux units, which typically corresponds to a temperature of ≈ 100 nK, the SQUID is reset. The temperature range can be greatly expanded if the reset events are carefully tracked and counted, either by a computer running appropriate software or by a dedicated piece of hardware.

While adequate for many applications, the conventional scheme has drawbacks: If the temperature is changed rapidly or the temperature noise is high, the counting hardware and/or software loses flux count. In the case of a software counter, the temperature reading is lost entirely if the software is reset or restarted. In the case of a multiplexed SQUID controller, these drawbacks become more severe because flux readings are taken less frequently.



A Branch Containing a Secondary SQUID would be added to a single-SQUID HRT circuit. The secondary SQUID would register a small fraction of the flux passing through the primary SQUID.

The proposed scheme is intended to eliminate these drawbacks. The scheme calls for including a secondary SQUID and its readout instrumentation that would register a small fraction of the magnetic flux passing through a primary SQUID. The scheme includes the following elements:

- Winding a secondary coil of fewer turns around the core to a second readout; or
- Forming a circuit branch parallel to the main coil with the secondary SQUID input coil in series with a large (compared to the SQUID input coil inductance) inductor; or

- Forming a circuit branch parallel to the main coil with a large inductor in series with a SQUID input coil shunted by a small inductor (see figure).

The goal is to avoid having to reset the secondary SQUID in the temperature range of interest, while maintaining the capability of determining the flux state of the primary SQUID unambiguously. If the secondary SQUID readout were monitored by a 16-bit data-acquisition board and the digitization effected by the board determined the readout accuracy, then the dynamic range afforded by this scheme could be optimized by designing the secondary

SQUID readout to be about 1/32,000 as sensitive as is the primary SQUID readout. In a typical application, this level of secondary-SQUID sensitivity would correspond to a temperature range ≈ 3 mK. In this temperature range, there would be no need to actively track the flux state to maintain fidelity of the readout. To avoid the need for counting hardware altogether, a tertiary readout could be added.

This work was done by Konstantin Penanen of Caltech for NASA's Jet Propulsion Laboratory. Further information is contained in a TSP (see page 1). NPO-41757



Error Rates and Channel Capacities in Multipulse PPM

It is now possible to compare expected performances of candidate modulation schemes.

NASA's Jet Propulsion Laboratory, Pasadena, California

A method of computing channel capacities and error rates in multipulse pulse-position modulation (multipulse PPM) has been developed. The method makes it possible, when designing an optical PPM communication system, to determine whether and under what conditions a given multipulse PPM scheme would be more or less advantageous, relative to other candidate modulation schemes.

In conventional M -ary PPM, each symbol is transmitted in a time frame that is divided into M time slots (where M is an integer >1), defining an M -symbol alphabet. A symbol is represented by transmitting a pulse (representing "1") during one of the time slots and no pulse (representing "0") during the other $M - 1$ time slots. Multipulse PPM is a generalization of PPM in which pulses are transmitted during two or more of the M time slots. If the number of pulses per symbol is n , then the number of symbols in the

alphabet is given by the binomial coefficient

$$C_n^M = M!/[n!(M-n)!].$$

The method is based partly on an analysis of the conditional probability, $p_1(y)$ or $p_0(y)$, that the actual value, y , of the noisy signal detected in a receiver during a given time slot represents a transmitted 1 or a transmitted 0, respectively. For purposes of the analysis, the signal-propagation channel is assumed to be memoryless. The analysis includes consideration of $L(y) = p_1(y)/p_0(y)$, defined as the likelihood ratio for receiving value y during the time slot. It is assumed that $L(y)$ is finite and, as is true for many channels of practical interest, that $L(y)$ increases monotonically with y . This analysis leads to a maximum-likelihood (ML) decision rule to be used by the receiver. The rule turns out to be equivalent to

the intuitive conjecture that the symbol most likely to have been transmitted, given the actual signal values detected during a symbol frame, is the one represented by 1 in each of the n time slots for which the detected signal values were the largest.

Next, an analysis of the probabilities that ML decisions are correct or incorrect for various detected signal levels leads to the following equation for the symbol error rate (SER) — that is, the probability of incorrect symbol detection:

$$SER = \sum_{s=0}^{\infty} \sum_{v=0}^{M-n} \sum_{t=1}^n I(t,v) C_t^n p_1(s)^t [1 - P_1(s)]^{n-t} C_v^{M-n} p_0(s)^v P_0(s-1)^{M-n-v},$$

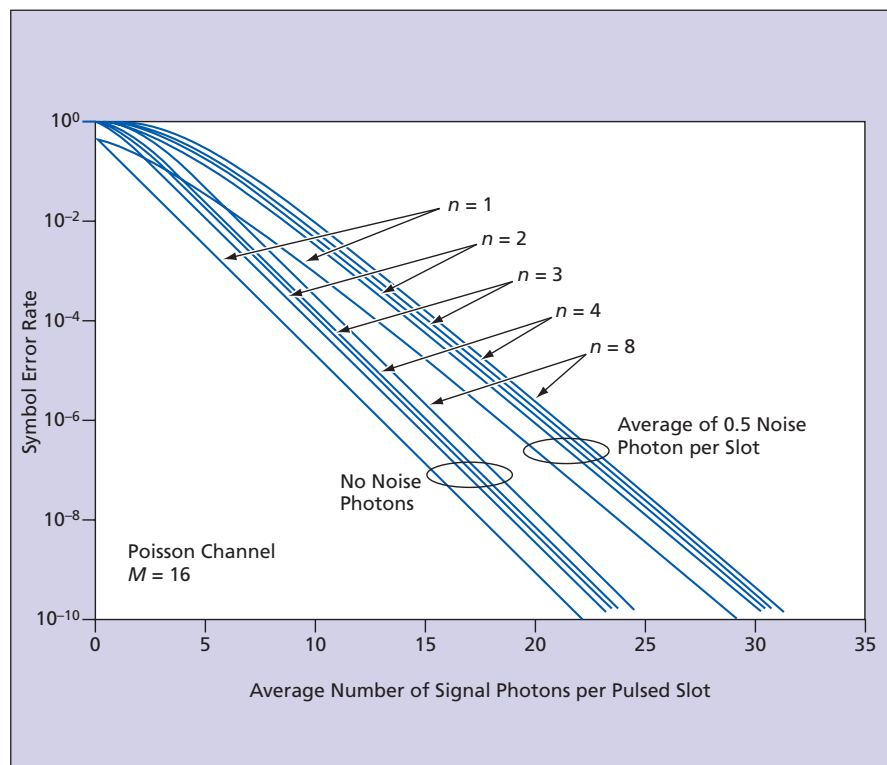
where $I(t,v) \equiv 1/C_t^{t+v}$, $P_1(s)$ is the probability that the digitized value of the detected signal (e.g., the number of detected photons) in a "1" slot is less than or equal to s , and $P_0(s)$ is the probability that the digitized value of the detected signal in a "0" slot is less than or equal to s . The figure presents an example of SER values calculated by use of these equations.

Next, a comparative analysis of throughput achievable in conventional and multipulse PPM under bandwidth, average-power, and peak-power constraints leads to the following equation for the channel capacity:

$$C = \frac{n}{M} E_{Y|X=1} \log \frac{p_1(Y)}{p(Y)} + \frac{M-n}{M} E_{Y|X=0} \log \frac{p_0(Y)}{p(Y)} \text{ bits/slot,}$$

where $p(Y) \equiv (n/M)p_1(Y) + [(M-n)/M]p_0(Y)$ is denoted the probability mass function for a randomly chosen slot and $E_{Y|X=1}$ or $E_{Y|X=0}$ is the expected value of signal level Y in a slot for which the transmitted signal value, X , was 1 or 0, respectively.

This work was done by Jon Hamkins and Bruce Moision of Caltech for NASA's Jet Propulsion Laboratory. For further information, contact iaoffice@jpl.nasa.gov. NPO-41536



SER Values were calculated for 16-ary PPM using several different values n and two different noise levels in a Poisson channel.

Σ Two Mathematical Models of Nonlinear Vibrations

Model parameters are fit to empirical vibration data.

NASA's Jet Propulsion Laboratory, Pasadena, California

Two innovative mathematical models of nonlinear vibrations, and methods of applying them, have been conceived as byproducts of an effort to develop a Kalman filter for highly precise estimation of bending motions of a large truss structure deployed in outer space from a space-shuttle payload bay. These models are also applicable to modeling and analysis of vibrations in other engineering disciplines, on Earth as well as in outer space.

The first model is denoted the amplitude-dependent stiffness (ADS) model to emphasize the difference between it and the classical linear harmonic-oscillator model, in which stiffness is a constant. The ADS model is embodied in the equation

$$\ddot{x} + \xi \dot{x} + K(x, \dot{x})x = 0,$$

where x is the instantaneous amplitude of the oscillating position or modal coordinate, ξ is a damping parameter, and $K(x, \dot{x})$ is the ADS.

In the initial outer-space application, the ADS was represented by the following nonlinear function:

$$K(x, \dot{x}) = a + bA(x, \dot{x}) + cA(x, \dot{x})^2,$$

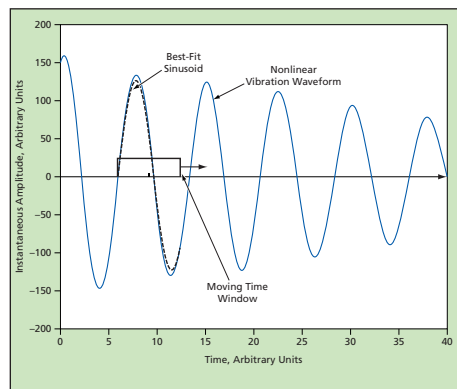
where a , b , and c are constant parameters to be obtained by fitting the model to empirical amplitude-versus-frequency data, and $A(x, \dot{x})$ is a modal amplitude. The amplitude-versus-frequency data are obtained by means of a moving-window estimation technique in which one analyzes the instantaneous vibration waveform during a time window of about 90 percent of the

time-average vibration period. The amplitude and frequency are taken to be those of a sinusoid that makes the least-squares best fit to the instantaneous amplitude during the window (see figure). The window is then moved by about 2 percent of the average period and another best-fit sinusoid is found. This process is repeated until a suitably representative sample of the vibration waveform has been acquired.

The modal amplitude is given by

$$A(x, \dot{x}) = \sqrt{x^2 + \left(\frac{\dot{x}}{\bar{K}(x, \dot{x})}\right)^2},$$

where $\bar{K}(x, \dot{x})$ is any reasonable approx-



A Nonlinear Decaying Waveform is approximated with a best-fit sinusoid during a moving window. The resulting sinusoidal amplitude and frequency data are collected from fits for the entire sequence of window positions and used to characterize the frequency versus amplitude of the nonlinear waveform. These frequency versus amplitude data are then fit to an amplitude-dependent stiffness (ADS) representation.

imation of $K(x, \dot{x})$. One can refine the approximation iteratively, starting from $K(x, \dot{x}) = a$, then using the resulting value of $A(x, \dot{x})$ in computing a value of $\bar{K}(x, \dot{x})$ by use of the above equation for $K(x, \dot{x})$.

The second model, denoted the moment-expansion (ME) model, is embodied in the equation

$$\dot{x} + M(x, \dot{x}) = 0,$$

where the function $M(x, \dot{x})$ is a moment expansion that captures damping and stiffness effects. The moment expansion is given by

$$M(x, \dot{x}) = \sum_{j=0}^3 \sum_{i=0}^3 p_{ij} x^i \dot{x}^j,$$

where both i and j range from 0 to 3, except that there is no $(i, j) = (0, 0)$ term. In the original outer-space application, the parameters p_{ij} are obtained from (1) modal position and velocity estimates obtained from Kalman-filter states and (2) derived accelerations.

In a test relevant to the original outer-space application, the ADS and ME models were compared with each other, with a linear model, and with a prior nonlinear model known as the Duffing model. The ADS model was found to yield the least error.

This work was done by Paul Brugarolas, David Bayard, John Spanos, and William Breckenridge of Caltech for NASA's Jet Propulsion Laboratory. For further information, contact iaoffice@jpl.nasa.gov. NPO-41360

Σ Simpler Adaptive Selection of Golomb Power-of-Two Codes

The selected code-parameter value is within 1 of the optimum value.

NASA's Jet Propulsion Laboratory, Pasadena, California

An alternative method of adaptive selection of Golomb power-of-two (GPO2) codes has been devised for use in efficient, lossless encoding of sequences of non-negative integers from discrete sources. The method is intended especially for use in compression of digital image data. This method is somewhat suboptimal, but offers the advantage in

that it involves significantly less computation than does a prior method of adaptive selection of optimum codes through "brute force" application of all code options to every block of samples.

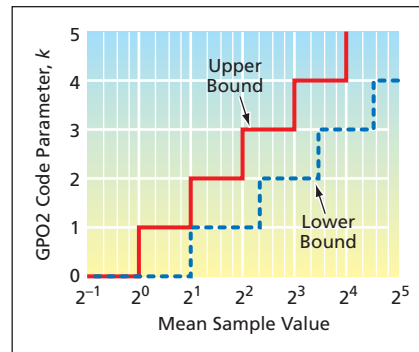
A rather lengthy discussion of background is necessary to give meaning to a brief summary of this innovation. For positive integer, m , the m th Golomb

code defines a reversible, prefix-free mapping of non-negative integers to variable-length binary code words. Golomb codes are optimum for geometrically distributed sources (a model that frequently arises in image compression): In the case of a geometrically distributed random variable, δ , the appropriately selected Golomb code minimizes the ex-

pected code-word length over all possible lossless binary codes for δ .

In a GPO2 code, $m = 2^k$, where k is a non-negative integer. Such a code makes the coding process particularly simple: The code word for the integer δ consists of the unary representation of $\lfloor \delta/2^k \rfloor$ (that is, $\lfloor \delta/2^k \rfloor$ zeros followed by a one) concatenated with the k least significant bits of the binary representation of δ . More specifically, the code is called a GPO2 code of parameter k .

The problem is to calculate or estimate the value of code parameter k that minimizes the expected bit rate (the average number of encoded bits per source symbol) for an image or other source. This problem arises in Rice coding, which is a coding method well known among experts in data compression. The Rice algorithm encodes a block of samples by use of the best code option for the block from among several candidate codes that consist mostly of different GPO2 codes. A fixed number of bits are used preceding the encoded block to indicate which code was selected. The Rice method does not spec-



Upper and Lower Bounds on the optimum value of the code parameter make it possible to reduce the number of code options that must be considered.

ify how to find the best code option, and the most common approach is to exhaustively try every code option to pick the best one for each block. Information from previously coded blocks is not utilized. This concludes the background information.

In the present method, unlike in the Rice method, one utilizes the mean sample value in each block. The method is based partly on a theoretical

derivation of bounds on the optimum value of k as functions of the mean sample value (see figure). These bounds are such that no more than three code choices can be optimum for a given mean sample value. For a given mean value, one of the three candidate codes is selected in a procedure that involves only integer arithmetic (without divisions) and table look-ups. It has been shown that the value of k selected in this relatively simple procedure is always within 1 of the optimum k value for the source, and that the cost added by the suboptimality of the selection is never more than 1/2 bit per sample and no more than about 13-percent inefficiency. In practical image compression experiments, the cost added by the suboptimality of the selection is negligible.

This work was done by Aaron Kiely of Caltech for NASA's Jet Propulsion Laboratory.

The software used in this innovation is available for commercial licensing. Please contact Karina Edmonds of the California Institute of Technology at (626) 395-2322. Refer to NPO-41336.



VCO PLL Frequency Synthesizers for Spacecraft Transponders

Two documents discuss a breadboard version of advanced transponders that, when fully developed, would be installed on future spacecraft to fly in deep space. These transponders will be required to be capable of operation on any deep-space-communications uplink frequency channel between 7,145 and 7,235 MHz, and any downlink frequency channel between 8,400 and 8,500 MHz. The document focuses on the design and operation of frequency synthesizers for the receiver and transmitter. Heretofore, frequency synthesizers in deep-space transponders have been based on dielectric resonator oscillators (DROs), which do not have the wide tuning bandwidth necessary to tune over all channels in the uplink or downlink frequency bands. To satisfy the requirement for tuning bandwidth, the present frequency synthesizers are based on voltage-controlled-oscillator (VCO) phase-locked loops (PLLs) implemented by use of monolithic microwave integrated circuits (MMICs) implemented using InGaP heterojunction bipolar transistor (HBT) technology. MMIC VCO PLL frequency synthesizers similar to the present ones have been used in commercial and military applications but, until now, have exhibited too much phase noise for use in deep-space transponders. The present frequency synthesizers contain advanced MMIC VCOs, which use HBT technology and have lower levels of flicker (1/f) phase noise. When these MMIC VCOs are used with high-speed MMIC frequency dividers, it becomes possible to obtain the required combination of frequency agility and low phase noise.

This work was done by Scott Smith, Narayan Mysoor, James Lux, and Brian Cook of Caltech for NASA's Jet Propulsion Laboratory. For further information, contact iaoffice@jpl.nasa.gov. NPO-42909

Wide Tuning Capability for Spacecraft Transponders

A document presents additional information on the means of implementing a capability for wide tuning of microwave receiver and transmitter

frequencies in the development reported in the immediately preceding article, "VCO PLL Frequency Synthesizers for Spacecraft Transponders" (NPO-42909). The reference frequency for a PLL-based frequency synthesizer is derived from a numerically controlled oscillator (NCO) implemented in digital logic, such that almost any reference frequency can be derived from a fixed crystal reference oscillator with microhertz precision. The frequency of the NCO is adjusted to track the received signal, then used to create another NCO frequency used to synthesize the transmitted signal coherent with, and at a specified frequency ratio to, the received signal. The frequencies can be changed, even during operation, through suitable digital programming.

The NCOs and the related tracking loops and coherent turnaround logic are implemented in a field-programmable gate array (FPGA). The interface between the analog microwave receiver and transmitter circuits and the FPGA includes analog-to-digital and digital-to-analog converters, the sampling rates of which are chosen to minimize spurious signals and otherwise optimize performance. Several mixers and filters are used to properly route various signals.

This work was done by James Lux, Narayan Mysoor, Biren Shah, Brian Cook, and Scott Smith of Caltech for NASA's Jet Propulsion Laboratory. For further information, contact iaoffice@jpl.nasa.gov. NPO-43000

Adaptive Deadband Synchronization for a Spacecraft Formation

A paper discusses general problems in estimation and control of the states (positions, attitudes, and velocities) of spacecraft flying in formation, then addresses the particular formation-flying-control problem of synchronization of deadbands. The paper presents a deadband-synchronization algorithm for the case in which the spacecraft are equipped with pulse-width-modulated thrusters for maintaining their required states. The algorithm synchronizes thruster-firing times across all six degrees of freedom of all the spacecraft. The algorithm is scalable, inherently adapts to disturbances, and does not require knowledge of space-

craft masses and disturbance forces. In this algorithm, one degree of freedom of one spacecraft is designated the leader, and all other degrees of freedom of all spacecraft as followers. The Cassini adaptive optimum deadband drift controller is the subalgorithm for control in each degree of freedom, and the adaptation is run until each spacecraft achieves a specified drift period. The adaptation is critical because a different disturbance affects each different degree of freedom. Then the leader communicates its thruster-firing starting times to the followers. Then, for each follower, a deadband-synchronization subalgorithm determines the shift needed to synchronize its drift period with that of the leader.

This work was done by Daniel Scharf, Fred Hadaegh, and Bryan Kang of Caltech for NASA's Jet Propulsion Laboratory.

The software used in this innovation is available for commercial licensing. Please contact Karina Edmonds of the California Institute of Technology at (626) 395-2322. Refer to NPO-43258.

Analysis of Performance of Stereoscopic-Vision Software

A team of JPL researchers has analyzed stereoscopic vision software and produced a document describing its performance. This software is of the type used in maneuvering exploratory robotic vehicles on Martian terrain. The software in question utilizes correlations between portions of the images recorded by two electronic cameras to compute stereoscopic disparities, which, in conjunction with camera models, are used in computing distances to terrain points to be included in constructing a three-dimensional model of the terrain. The analysis included effects of correlation-window size, a pyramidal image down-sampling scheme, vertical misalignment, focus, maximum disparity, stereo baseline, and range ripples. Contributions of sub-pixel interpolation, vertical misalignment, and foreshortening to stereo correlation error were examined theoretically and experimentally. It was found that camera-calibration inaccuracy contributes to both down-range and cross-range error but stereo correlation error affects only the down-range error. Experimental data for quantifying

the stereo disparity error were obtained by use of reflective metrological targets taped to corners of bricks placed at known positions relative to the cameras. For the particular 1,024-by-768-pixel cameras of the system analyzed, the standard deviation of the down-range disparity error was found to be 0.32 pixel.

*This work was done by Won Kim, Adnan Ansar, Robert Steele, and Robert Steinke of Caltech for NASA's Jet Propulsion Laboratory. For further information, contact iaoffice@jpl.nasa.gov
NPO-42487*

Estimating the Inertia Matrix of a Spacecraft

A paper presents a method of utilizing some flight data, aboard a spacecraft that includes reaction wheels for attitude control, to estimate the inertia matrix of the spacecraft. The required data are digitized samples of (1) the spacecraft attitude in an inertial reference frame as measured, for example, by use of a star tracker and (2) speeds of rotation of the reaction wheels, the moments of inertia of which are deemed to be known.

Starting from the classical equations for conservation of angular momentum of a rigid body, the inertia-matrix-estimation problem is formulated as a constrained least-squares minimization problem with explicit bounds on the inertia matrix incorporated as linear matrix inequalities. The explicit bounds reflect physical bounds on the inertia matrix and reduce the volume of data that must be processed to obtain a solution. The resulting minimization problem is a semidefinite optimization problem that can be solved efficiently, with guaranteed convergence to the global optimum, by use of readily available algorithms. In a test case involving a model attitude platform rotating on an air bearing, it is shown that, relative to a prior method, the present method produces better estimates from few data.

This work was done by Behçet Açıkmese, Jason Keim, and Joel Shields of Caltech for NASA's Jet Propulsion Laboratory.

The software used in this innovation is available for commercial licensing. Please contact Karina Edmonds of the California Institute of Technology at (626) 395-2322. Refer to NPO-43631.

Spatial Coverage Planning for Exploration Robots

A report discusses an algorithm for an onboard planning and execution technology to support the exploration and characterization of geological features by autonomous rovers. A rover that is capable of deciding which observations are more important relieves the engineering team from much of the burden of attempting to make accurate predictions of what the available rover resources will be in the future. Instead, the science and engineering teams can uplink a set of observation requests that may potentially oversubscribe resources and let the rover use observation priorities and its current assessment of available resources to make decisions about which observations to perform and when to perform them.

The algorithm gives the rover the ability to model spatial coverage quality based on data from different scientific instruments, to assess the impact of terrain on coverage quality, to incorporate user-defined priorities among subregions of the terrain to be covered, and to update coverage quality rankings of observations when terrain knowledge changes. When the rover is exploring large geographical features such as craters, channels, or boundaries between two different regions, an important factor in assessing the quality of a mission plan is how the set of chosen observations spatially cover the area of interest. The algorithm allows the rover to evaluate which observation to perform and to what extent the candidate observation will increase the spatial coverage of the plan.

This work was done by Daniel Gaines, Tara Estlin, and Caroline Chouinard of Caltech for NASA's Jet Propulsion Laboratory.

The software used in this innovation is available for commercial licensing. Please

contact Karina Edmonds of the California Institute of Technology at (626) 395-2322. Refer to NPO-44282.

Increasing the Life of a Xenon-Ion Spacecraft Thruster

A short document summarizes the re-design of a xenon-ion spacecraft thruster to increase its operational lifetime beyond a limit heretofore imposed by nonuniform ion-impact erosion of an accelerator electrode grid. A peak in the ion current density on the centerline of the thruster causes increased erosion in the center of the grid. The ion-current density in the NSTAR thruster that was the subject of this investigation was characterized by peak-to-average ratio of 2:1 and a peak-to-edge ratio of greater than 10:1. The redesign was directed toward distributing the same beam current more evenly over the entire grid and involved several modifications of the magnetic-field topography in the thruster to obtain more nearly uniform ionization. The net result of the redesign was to reduce the peak ion current density by nearly a factor of two, thereby halving the peak erosion rate and doubling the life of the thruster. (Note: NSTAR stands for NASA SEP Technology Application Readiness; SEP stands for solar electric propulsion.)

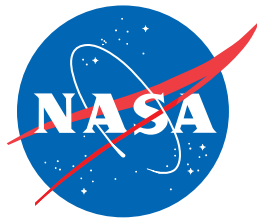
This work was done by Dan Goebel, James Polk, Anita Sengupta, and Richard Wirz of Caltech for NASA's Jet Propulsion Laboratory. Further information is contained in a TSP (see page 1). In accordance with Public Law 96-517, the contractor has elected to retain title to this invention. Inquiries concerning rights for its commercial use should be addressed to:

*Innovative Technology Assets Management
JPL*

*Mail Stop 202-233
4800 Oak Grove Drive
Pasadena, CA 91109-8099
(818) 354-2240*

E-mail: iaoffice@jpl.nasa.gov

Refer to NPO-43495, volume and number of this NASA Tech Briefs issue, and the page number.



National Aeronautics and
Space Administration